



Probabilistic precipitation downscaling for ungauged mountain sites: a pilot study for the Hindu Kush Himalaya

Marc Girona-Mata^{1,2}, Andrew Orr¹, Martin Widmann³, Daniel Bannister⁴, Ghulam Hussain Dars⁵, Scott Hosking^{1,6}, Jesse Norris⁷, David Ocio⁸, Tony Phillips¹, Jakob Steiner^{9,10}, and Richard E. Turner²

¹British Antarctic Survey, UK Research and Innovation, Cambridge, UK

²Department of Engineering, University of Cambridge, Cambridge, UK

³School of Geography, Earth and Environmental Sciences, University of Birmingham, Birmingham, UK

⁴WTW Research Network, WTW, London, UK

⁵U.S.-Pakistan Center for Advanced Studies in Water, Mehran University of Engineering and Technology, Jamshoro, Pakistan

⁶The Alan Turing Institute, London, UK

⁷Atmospheric and Oceanic Sciences, University of California Los Angeles, Los Angeles, CA, USA

⁸Mott MacDonald, Cambridge, UK

⁹Institute of Geography and Regional Science, University of Graz, Graz, Austria

¹⁰Himalayan University Consortium, Lalitpur, Nepal

Correspondence: Marc Girona-Mata (mg963@cam.ac.uk)

Received: 6 September 2024 – Discussion started: 7 October 2024

Revised: 12 April 2025 – Accepted: 16 April 2025 – Published: 21 July 2025

Abstract. This study introduces a novel approach to post-processing (i.e. downscaling and bias-correcting) reanalysis-driven regional climate model daily precipitation outputs that can be generalised to ungauged mountain locations by leveraging sparse in situ observations and a probabilistic regression framework. We call this post-processing approach generalised probabilistic regression (GPR) and implement it using both generalised linear models and artificial neural networks (i.e. multi-layer perceptrons). By testing the GPR post-processing approach across three Hindu Kush Himalaya (HKH) basins with varying hydro-meteorological characteristics and four experiments, which are representative of real-world scenarios, we find it performs consistently much better than both raw regional climate model output and deterministic bias correction methods for generalising daily precipitation post-processing to ungauged locations. We also find that GPR models are flexible and can be trained using data from a single region or multiple regions combined together, without major impacts on model performance. Additionally, we show that the GPR approach results in superior skill for post-processing entirely ungauged regions, by leveraging data from other regions as well as ungauged high-elevation ranges. This suggests that GPR models have po-

tential for extending post-processing of daily precipitation to ungauged areas of HKH. Whilst multi-layer perceptrons yield marginally improved results overall, generalised linear models are a robust choice, particularly for data-scarce scenarios, i.e. post-processing extreme precipitation events and generalising to completely ungauged regions.

1 Introduction

The mountain ranges of High Mountain Asia, often referred to as the Water Towers of Asia (Immerzeel et al., 2010), are the source of many major rivers in South Asia, such as the Indus or the Ganges, supplying water resources to a rich diversity of terrestrial and marine ecosystems (Xu et al., 2019) and to approximately 2 billion people living in or directly downstream of them (Bolch et al., 2012; Mukherji et al., 2019; Wester et al., 2019; Widmann et al., 2019). These resources are heavily reliant on precipitation caused primarily by large-scale atmospheric circulations, such as the Indian summer monsoon and winter westerly disturbances, interacting with the steep orography that characterises the southern rim of High Mountain Asia, comprising the Hindu

Kush Himalaya (HKH) mountain ranges (Bookhagen and Burbank, 2010; Palazzi et al., 2013; Baudouin et al., 2020; Dimri et al., 2015). Yet, despite the large human populations depending on these resources for power, industry, tourism, farming and domestic consumption, the contributions of rain and snow (and its ensuing melt) to these river systems are still poorly studied and little understood. This precipitation knowledge gap in HKH severely affects our ability to quantify its present-day water resources and associated stream flows (Immerzeel et al., 2015; Arfan et al., 2019; Li et al., 2018; Salzmänn et al., 2014). Consequently, it constitutes the largest source of uncertainty when it comes to making effective and robust water management decisions (e.g. water infrastructure construction, water demand management) and their critical role in regulating regional water supply, as well as planning for the hydrological impacts of climate change (Chinnasamy et al., 2015; Mombloch et al., 2019; Wester et al., 2019; Nie et al., 2021; Orr et al., 2022).

Improving our understanding of precipitation in the HKH region is highly challenging (e.g. Wester et al., 2019; Sabin et al., 2020; Orr et al., 2022). In particular, the extreme orography that characterises this region results in large precipitation variations over small spatio-temporal scales, which are poorly understood due to the sparse and uneven rain and snow gauge network across the region (Archer and Fowler, 2004; Bannister et al., 2019; Immerzeel et al., 2015; Bookhagen and Burbank, 2010; Baudouin et al., 2020; Pritchard, 2021). For example, an area of around 566 000 km² above 4000 m elevation in HKH is currently represented by a single long-running gauge station in the Global Historical Climatology Network database (Pritchard, 2021). This poor understanding of precipitation extends to localised extremes that result from the triggering of convective events by small-scale topographic features (Orr et al., 2017; Bhardwaj et al., 2021; Ren et al., 2017; Dimri et al., 2017; Thayyen et al., 2013; Potter et al., 2018), which are often associated with rapid hydrological responses as well as hydro-meteorological hazards such as floods and landslides (Qazi et al., 2019; Lutz et al., 2016; Ji et al., 2020; Dimri et al., 2017; Thayyen et al., 2013; Das et al., 2006).

One of the approaches to overcome the issues related to the limited gauge networks in HKH has been to develop daily gridded datasets with wide spatial and temporal coverage. These include gauge-based products such as the Asian Precipitation Highly Resolved Observational Data Towards Evaluation of Water Resources (APHRODITE; Yatagai et al., 2012), satellite-based products such as the Tropical Rainfall Measuring Mission (TRMM; Huffman et al., 2007), climate reanalysis products such as ECMWF Reanalysis v5 (ERA5; Hersbach et al., 2020) and multi-source products such as the Multi-Source Weighted-Ensemble Precipitation (MSWEP; Beck et al., 2019), which merges gauge, satellite and reanalysis data. However, in HKH these datasets are characterised by large differences in both climatological and extreme precipitation values, with the lack of consensus confirming that our

understanding of precipitation characteristics in this region is extremely poor (Bannister et al., 2019; Palazzi et al., 2013; Li et al., 2018). The large differences between these datasets are explained by the different types of observations used in them, as well as the methods used to compile them. For example, APHRODITE relies on distance-weighted interpolation of gauge values to derive precipitation patterns, which are difficult to robustly calculate in HKH due to the lack of in situ observations, as well as the large spatio-temporal precipitation gradients (Bannister et al., 2019; Ji et al., 2020; Luo et al., 2020; Andermann et al., 2011). A recent alternative, MSWEP (Beck et al., 2019), which is arguably one of the best global precipitation datasets, also relies on gauge data and is therefore much less well constrained to observations in HKH compared with elsewhere. Consequently, alternative tools are needed to better understand the detailed spatio-temporal characteristics of precipitation in HKH.

Dynamic downscaling of coarse spatial resolution reanalysis datasets (e.g. approximately 30 km for ERA5) using a regional climate model (RCM) is increasingly being used to produce high-resolution gridded precipitation products over HKH (Norris et al., 2020; Bannister et al., 2019; Maussion et al., 2011; Wang et al., 2021). These RCMs are characterised by spatial resolutions from 1–10 km that are generally able to resolve the complex terrain and thus better represent precipitation variability, and especially extremes. However, RCM outputs are still subject to errors and uncertainty (Giorgi, 2019), which can be exacerbated in mountain areas due to the complexity of the terrain (Sanjay et al., 2017; ul Hasson et al., 2019). For example, while reanalysis-driven RCM simulations are able to capture the large-scale circulation accurately (e.g. summer monsoon and westerly disturbances) by using either nudging or frequent initialisation techniques (Norris et al., 2020; Bannister et al., 2019; Maussion et al., 2011; Wang et al., 2021), they can still be subject to deficiencies in the representation of key physical processes such as the local valley wind regime, boundary layer and cloud microphysics (Orr et al., 2017; Potter et al., 2018), as well as discrepancies between real and simulated orography (Eden et al., 2012). Statistical post-processing techniques, such as bias correction, are therefore often applied to improve the accuracy of RCM outputs, including precipitation (e.g. Shrestha et al., 2017; Bannister et al., 2019; Dimri, 2021; Tazi et al., 2024).

The model output statistics (MOS) approach to bias-correcting RCM simulations involves developing statistical relationships between RCM outputs, used as predictors, and observations, used as predictands (e.g. Klein and Glahn, 1974; Maraun and Widmann, 2018). MOS post-processing methods are usually deployed in either single-site or multi-site fashion to correct RCM simulations for locations where observations are available. However, in settings where gauge measurements are spatially sparse, MOS post-processing can also be used to adjust RCM precipitation outputs at ungauged locations (e.g. Samuel et al., 2012). In regions such as HKH

where standard spatial interpolation techniques fail to capture the local-scale spatio-temporal precipitation variability, such an approach is fundamental; yet it has not received much attention in the past. Bannister et al. (2019) applied bias correction to ungauged locations by using a deterministic distribution-wise MOS method to adjust RCM precipitation outputs across two Himalayan basins. Additionally, MOS post-processing for bias correction can sometimes also involve downscaling RCM outputs to higher spatial resolutions (i.e. they correct for biases as well as downscale from a coarser to a finer scale). Hereafter, we use the term post-processing to refer to the combination of downscaling and bias-correcting.

Traditional MOS methods post-process the marginal distribution of the RCM output deterministically. In this setting, a specific set of predictors always yields the same corrected value and the spatio-temporal structure of the simulated output is not explicitly altered. This implicitly assumes that local-scale spatio-temporal variability is completely captured by the RCM-simulated grid box variability. Whilst this assumption might hold in the case of pure bias correction, if the post-processing also involves downscaling to point observations (or higher-resolution gridded data) then deterministic approaches are not appropriate and a probabilistic method should be used instead (Maraun, 2013).

Furthermore, using regression-based MOS methods, the synchrony (or pairwise correspondence) between reanalysis-driven RCMs and observations can be leveraged to correct for biases in the temporal representation of RCM precipitation outputs, which can often be large (Lafon et al., 2013). In settings where the pairwise correspondence between RCM hindcasts and observations is low, such as in HKH, probabilistic regression-based MOS methods can also provide value by characterising predictive uncertainty.

Previous studies have developed regression-based MOS methods based on artificial neural networks to statistically post-process precipitation data (e.g. Cannon, 2008; Sachindra et al., 2018; Baño-Medina et al., 2020; Vaughan et al., 2022). For example, the multi-site precipitation downscaling framework proposed by Cannon (2008) employs artificial neural networks for probabilistic regression. More advanced regression-based MOS model architectures have also been leveraged recently to undertake this task, including convolutional neural networks (Baño-Medina et al., 2020), autoencoders (Vandal et al., 2019) and neural processes (Vaughan et al., 2022). However, all these methods generally rely on the availability of abundant training data and thus focus on data-rich regions. The potential of regression-based MOS post-processing for ungauged mountain locations (such as in HKH) remains untapped.

In this pilot study, we introduce a generalised probabilistic regression (GPR) MOS approach for post-processing (i.e. downscaling and bias-correcting) RCM daily precipitation outputs using sparse gauge data in HKH. This approach extends the pairwise stochastic MOS framework proposed by

Wong et al. (2014) and leverages probabilistic regression models (i.e. generalised linear models and multi-layer perceptrons). The key advantage of the GPR approach is that it is capable of generalising to ungauged locations, whilst also capturing the uncertainty that arises both from this spatio-temporal generalisation and from the asynchronous timing of precipitation between RCM output and observations. Thus, using the GPR approach, we can leverage a discrete and relatively sparse network of in situ observations to improve precipitation maps (i.e. gridded products) for HKH whilst quantifying the uncertainty of our estimates. The GPR approach can also be viewed as a probabilistic spatio-temporal interpolation technique for daily precipitation observations informed by (or conditioned on) RCM simulations and other contextual factors. Furthermore, the framework we employ is, in essence, a conditional MOS precipitation generator that is consistent with the RCM-simulated weather (Cannon, 2008; Wong et al., 2014).

We test the GPR framework by post-processing daily precipitation output from an RCM simulation of HKH produced using the Weather Research and Forecasting (WRF) model for three target regions, namely, the eastern and western reaches of the Upper Indus Basin and the central part of the Upper Ganges Basin, which hereafter are referred to as East UIB, West UIB and Central UGB, respectively (Fig. 1). Together, these three regions span a wide portion of HKH and have very different characteristics in terms of geography, orography, climatology and observational network/data availability, i.e. providing a diverse range of conditions/challenges for the GPR framework in order to robustly test it. Finally, although the focus of this study is HKH, the results of this exercise should be applicable to other data-sparse mountain ranges in the world.

2 Data and methods

2.1 Target regions and datasets

The West UIB region includes the Gilgit-Baltistan area, which is located in Karakoram and the western Himalaya (Fig. 1). The Gilgit-Baltistan area is 72 971 km² in size and includes the Hunza and Gilgit rivers, as well as the main branch of the Indus (Iqbal et al., 2019). For this study, the daily precipitation records available for this area were collected from 12 stations over the period 1995–2015 (comprising a total of 76 860 data points), which range from 1460 to 4707 m above sea level (m.a.s.l.) (Table 1). The average distance between neighbouring stations is around 60 km.

The East UIB region includes the Sutlej River basin and the Beas River basin, which are situated in the western Himalaya. The Sutlej River basin has an area of 60 803 km² (above the Bhakra Dam) and its river is the largest and easternmost of the tributaries of the Indus (Fig. 1). The Beas River basin has an area of 12 286 km² (above the Pong

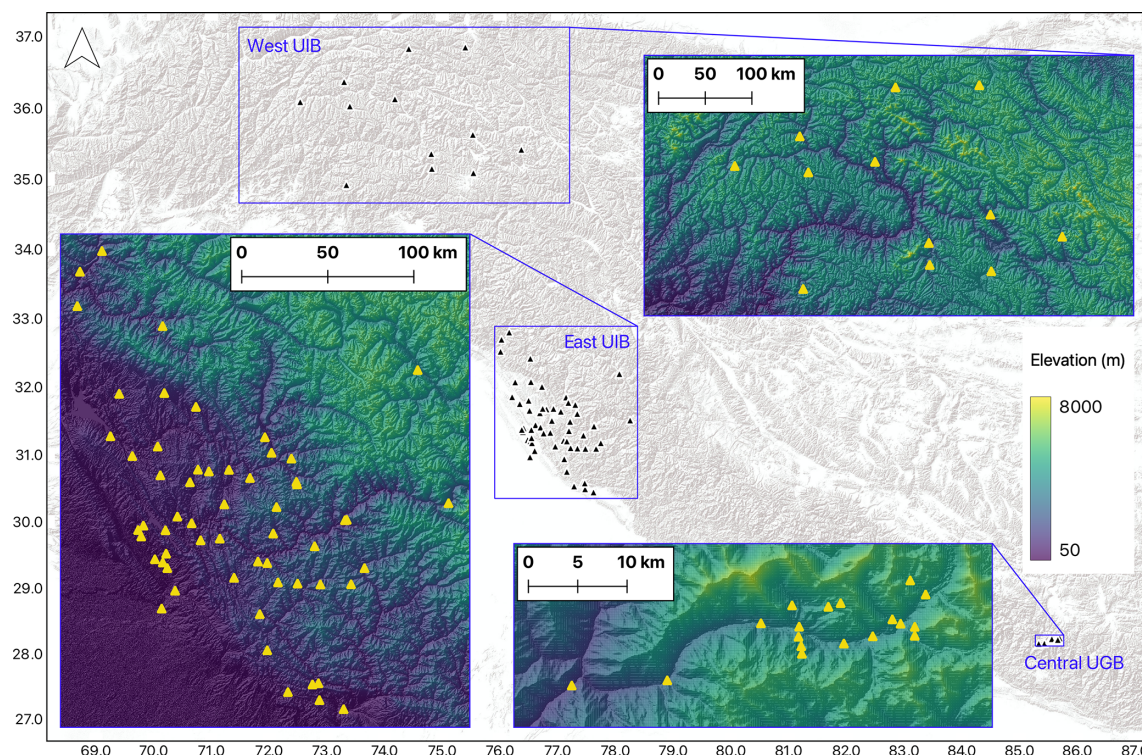


Figure 1. Map showing the three target regions across HKH: west Upper Indus Basin (West UIB), east Upper Indus Basin (East UIB) and central Upper Ganges Basin (Central UGB), including the location of the gauge measurements (black triangles). Inset maps show more detail for each of the target regions, including the elevation of the topography (shading) and the location of gauge measurements (yellow triangles). The topography dataset shown in the inset maps is from the Shuttle Radar Topography Mission (SRTM) digital elevation model.

Dam) and its river is itself a tributary of the Sutlej River. The available daily precipitation records in these basins (and neighbouring areas) come from 58 stations over the period 1980–2013 (364 713 data points), which range from 256 to 3645 m a.s.l. (Table 1). The majority of the stations are located in the lower reaches of these catchments (Fig. 1), i.e. a significant part of the catchment area sits at elevations above the highest monitoring station. The average distance between neighbouring stations is around 15 km; this constitutes a relatively dense network of precipitation measurements compared with West UIB, as well as many other areas in HKH (Nepal et al., 2023).

The Central UGB region includes the Langtang River catchment, which is situated in the central Himalaya (Fig. 1). It consists of a relatively small area and its river is a tributary to the Ganges (Fig. 1). The available daily precipitation records for this region come from 21 stations from 2012–2014 (15 152 data points), which range from 1406 to 5090 m a.s.l. (Table 1). The average distance between neighbouring stations is less than 2 km; this makes this one of the most dense networks of precipitation measurements in HKH (Steiner et al., 2021; Shea et al., 2015).

The WRF simulation is by Norris et al. (2019). It dynamically downscales 36 years of Climate Forecast System Reanalysis data (Saha et al., 2010) from 1979 to 2015 over

HKH at a spatial resolution of 6.7 km. We use multiple outputs (including daily precipitation) from this simulation from 1980 to 2014 that cover the three target regions (see Table 2). Norris et al. (2019) found that daily precipitation outputs from this simulation were better correlated with HKH gauge data in winter (correlation coefficient of 0.70) than in summer (correlation coefficient of 0.56). Additionally, over the Karakoram (West UIB), the simulated precipitation had a relatively substantial negative bias (Norris et al., 2017). Note that the station data described here and the WRF precipitation outputs are independent, i.e. the data were not assimilated into the Climate Forecast System Reanalysis. Finally, the terrain elevation of the three target regions (and stations) is taken from the Shuttle Radar Topography Mission (SRTM) digital elevation model, which has a spatial resolution of 30 m.

2.2 Generalised probabilistic regression (GPR) approach to MOS

The GPR approach to MOS post-processing involves predicting the probability distribution p of daily precipitation y , conditional on a set of predictors x , using regression models with parameters ϕ whose output variables characterise a

Table 1. Elevation range and summary of the stations used to provide daily precipitation observations for each of the three target regions. Note that each station contains gaps in the instrumental record.

Region	Elevation range (m a.s.l.)	No. stations	Period covered	No. data points
West UIB	1460–4707	12	1995–2014	76 860
East UIB	265–3645	58	1980–2013	364 713
Central UGB	1406–5090	20	2012–2014	15 152

stochastic process:

$$p_{\phi}(y|x) = p_{\phi}(y_1, y_2, \dots, y_m | x_1, x_2, \dots, x_m) \\ = \prod_{m=1}^M p_{\phi}(y_m | x_m). \quad (1)$$

Importantly, we assume that the probability distribution of daily precipitation at one spatio-temporal location is conditionally independent of that at all other spatio-temporal locations and thus the joint conditional probability $p(y|x)$ factorises into the product of $p(y_m|x_m)$, where m ranges from 1 to M and denotes a spatio-temporal location (i.e. there is a unique $m(s, t)$ for every combination of spatial location s and time t).

More concretely, the GPR approach uses regression models f_{ϕ} that map from inputs \mathbf{x}_m to outputs θ_m :

$$\theta_m = f_{\phi}(\mathbf{x}_m). \quad (2)$$

The input vector \mathbf{x}_m is D -dimensional, whereas the output vector θ_m is N -dimensional and explicitly parametrises the conditional probability distribution over daily precipitation y_m . We use three regression model architectures, namely, vector generalised linear models (VGLMs; Song, 2007) and two fully connected artificial neural networks, also referred to as multi-layer perceptrons (MLPs; Rumelhart et al., 1986).

In VGLMs, the mapping from inputs \mathbf{x}_m to outputs θ_m in Eq. (2) involves two key transformations. Firstly, a linear transformation, parametrised by a matrix of weights \mathbf{W}_1 , is applied to \mathbf{x}_m . Secondly, a non-linear transformation \mathbf{g} is subsequently applied to obtain the output vector θ_m . Note that each element θ_m^n is generated by applying a specific link function g_n , where n ranges from 1 to N and indexes each element of θ_m and \mathbf{g} . This element-wise non-linear transformation ensures that the resulting output values are valid parameters of the predicted probability distribution:

$$\theta_m = \mathbf{g}(\mathbf{W}_1^{\top} \mathbf{x}_m). \quad (3)$$

Thus, for VGLMs, parameters $\phi = \mathbf{W}_1$.

In contrast, in MLPs the mapping from inputs \mathbf{x}_m to outputs θ_m in Eq. (2) involves passing \mathbf{x}_m through multiple hidden layers, in sequence. The mapping from each layer to the next layer involves several linear transformations (determined by the number of units in that layer and parametrised

by matrices $\mathbf{W}_1, \mathbf{W}_2, \dots, \mathbf{W}_{H+1}$, where H is the number of layers), each followed by a non-linear activation function a :

$$\theta_m = \mathbf{g}(\mathbf{W}_2^{\top} a(\mathbf{W}_1^{\top} \mathbf{x}_m)). \quad (4)$$

This structure allows MLPs to model more complex (non-linear) relationships than a linear model. We use a very small MLP with one hidden layer of 10 units, where $\phi = \{\mathbf{W}_1, \mathbf{W}_2\}$ (Eq. 4; hereafter referred to as MLP_S) and a larger version with two hidden layers of 50 units each, where $\phi = \{\mathbf{W}_1, \mathbf{W}_2, \mathbf{W}_3\}$ (hereafter referred to as MLP_L):

$$\theta_m = \mathbf{g}(\mathbf{W}_3^{\top} a(\mathbf{W}_2^{\top} a(\mathbf{W}_1^{\top} \mathbf{x}_m))). \quad (5)$$

Rectified linear unit (ReLU) non-linearities are used as hidden layer activations a in both MLP architectures, except for the last layer, which also employs a vector of link functions \mathbf{g} to map each output variable.

In order to post-process WRF daily precipitation outputs, the three GPR model architectures use an input vector \mathbf{x}_m that consists of the $D = 26$ variables listed in Table 2, i.e. resulting in a 26-dimensional vector. This includes outputs from the WRF simulation at some spatio-temporal location m , as well as other context variables relating to the geographical location, orography and date. The outputs from the WRF simulation include daily precipitation (i.e. the variable that is being post-processed), as well as other variables that are closely related to precipitation, cloud properties and convective processes, such as convective available potential energy, cloud water vapour path, relative humidity, horizontal and vertical winds, and temperature.

To characterise the conditional probability over daily precipitation, we employ a Bernoulli–gamma mixture model, which is capable of jointly accounting for precipitation occurrence and magnitude and has been used in previous studies (Williams, 1998; Cannon, 2008). Precipitation occurrence is modelled by introducing a Bernoulli random variable r_m , which takes the value 1 with probability π_m and the value 0 with probability $1 - \pi_m$. When $r_m = 1$, precipitation magnitude y_m is modelled by a gamma distribution with parameters $\alpha \in (0, \infty)$ and $\beta \in (0, \infty)$. The Bernoulli–gamma mixture is implemented by specifying regression model architectures that generate an $N = 3$ dimensional output vector $\theta_m = [\pi_m, \alpha_m, \beta_m]$, using link functions $\mathbf{g} = [\text{sigmoid}(\cdot), \exp(\cdot), \exp(\cdot)]$. Further implementation details can be found in Appendix A.

Table 2. Summary of variables used as inputs to the GPR post-processing models, grouped by variable type.

Description	Symbol or abbreviation	Unit
WRF liquid and total precipitation	RAIN, PRECIP	mm d ⁻¹
WRF water vapour path	WVP	kg m ⁻² (daily average)
WRF convective available potential energy	CAPE	J kg ⁻¹ (daily average)
WRF temperature daily avg, max, min and range at 2 m	$T_{2\text{m}}, T_{2\text{m},\text{MAX}}, T_{2\text{m},\text{MIN}}, T_{2\text{m},\text{R}}$	K
WRF zonal and meridional wind at 10 m and 500 and 250 hPa	$U_{10\text{m}}, V_{10\text{m}}, U_{500}, V_{500}, U_{250}, V_{250}$	m s ⁻¹ (daily average)
WRF vertical wind at 500 and 250 hPa	W_{500}, W_{250}	m s ⁻¹ (daily average)
WRF relative humidity at 2 m and 500 hPa	$\text{RH}_{2\text{m}}, \text{RH}_{500}$	% (daily average)
WRF orography (based on surface geopotential height)	GPH	m
WRF land use index	LU	–
Latitude, longitude (of target station)	Y, X	m
Terrain elevation (of target station)	Z	m a.s.l.
Day of year encoded via sine and cosine functions	$\text{DoY}_{\text{SIN}}, \text{DoY}_{\text{COS}}$	–
Year	Year	–

2.3 Training, validation and testing

The GPR post-processing models are trained, validated and tested using the daily precipitation observations y^{obs} (Table 1) as predictands, i.e. target values. We employ a k -fold cross-validation approach, which involves splitting the data by location (i.e. station) into k folds, with $k - 2$ folds being used for training, 1 fold for validating and 1 fold for testing. This process is repeated k times, ensuring each fold is used once for testing. During training, we optimise the model parameters ϕ to maximise the average log-likelihood of the training dataset. For this, we use stochastic gradient descent with a batch size of 128 and the Adam optimiser (Kingma and Ba, 2015), with an initial learning rate equal to 10^{-3} . Here, we consider the validation step as part of the training process as it involves selecting, from the different model training iterations, the configuration of model parameters ϕ that maximises the average log-likelihood of the validation dataset, to avoid overfitting to the training data. We thus refer to the combined training and validation steps as training. Lastly, testing involves evaluating the performance of the trained models on the held-out locations in the test dataset.

2.4 Scaling factor approach

We compare the post-processed WRF precipitation results from the three GPR models against results obtained using a widely used deterministic MOS scaling factor approach (Maraun and Widmann, 2018), which we refer to as WRF_{SF} . Here, the raw WRF daily precipitation output for station s (hereinafter referred to as y_s^{WRF}) is scaled by the ratio between total observed daily precipitation ($\sum_{m=1}^M y_m^{\text{obs}}$) and total WRF-simulated daily precipitation ($\sum_{m=1}^M y_m^{\text{WRF}}$), where data points indexed $m \in \{1, \dots, M\}$ correspond to locations

other than s , to obtain $y_s^{\text{WRF}_{\text{SF}}}$:

$$y_s^{\text{WRF}_{\text{SF}}} = y_s^{\text{WRF}} \left(\frac{\sum_{m=1}^M y_m^{\text{obs}}}{\sum_{m=1}^M y_m^{\text{WRF}}} \right). \quad (6)$$

The scaling factor method is also applied using a 10-fold spatial cross-validation approach, where the scaling factor is derived using $k = 9$ folds (i.e. data points indexed $m \in \{1, \dots, M\}$) and then applied to the data points in the remaining fold.

2.5 Experiments

We undertake four experiments that assess the performance of the three GPR post-processing models, as well as the scaling factor approach WRF_{SF} . The four experiments represent increasingly complex (but realistic) ways of partitioning the available station data into subsets for training, validation and testing, and are shown schematically in Fig. 2. In Experiment 1 (hereafter referred to as E1), we train separate GPR models for each region (i.e. separate-region models) and test them by post-processing the WRF precipitation output at held-out locations within that region. This experiment represents a baseline scenario, where models are trained and tested for the same region. In Experiment 2 (E2), we train GPR models using data from all three regions combined (i.e. a combined-region model) and test them by post-processing WRF precipitation output at held-out locations within each of the regions. This experiment therefore explores whether training a model over a diverse range of regions/settings and then applying it to each of these regions outperforms the separate-region (E1) models. Both E1 and E2 use 10-fold cross-validation. Experiment 3 (E3) is similar to E2 but trains and validates the models on combined data from two regions (consisting of 80 % and 20 % of the combined data, respectively) and tests on 100 % of the data from a third, completely held-out, region. This experiment therefore explores whether a model

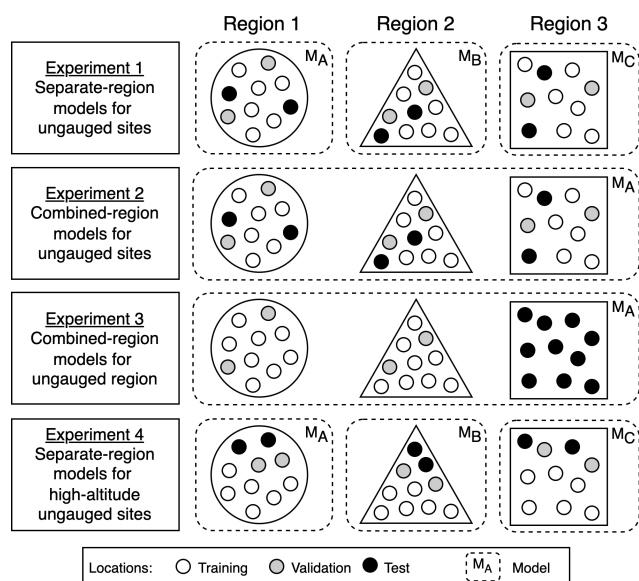


Figure 2. Schematic representation of the four experiments included in this study applied to three target regions. In Experiment 1, separate-region models for each of the three regions are trained and tested in held-out locations within each region. In Experiment 2, combined-region models are trained on data from all three regions and tested in held-out locations within those same regions. In Experiment 3, models are trained on two regions combined and tested in a third, completely held-out, region. Experiment 4 is analogous to Experiment 1 but held-out test locations are at higher elevations than those used for training and validation.

that is trained over a set of regions/settings can generalise to an entirely different new region. In E3 we use 3-fold cross-validation to ensure that each region is held-out for testing once to produce predictions for that region. Lastly, Experiment 4 (E4) is analogous to the separate-region (E1) experiment but splits the data up for training, validation and testing based on the elevation of the stations. Here, for each region, the top 10 % elevation stations are withheld for testing, the next 10 % are used for validation and the remaining 80 % (i.e. lowest elevation) stations are used for training. This experiment therefore explores whether models trained on data from the lower reaches of catchments, where the majority of stations are located, are capable of generalising to much higher elevations that are typically ungauged. Note that E4 does not therefore involve k -fold cross-validation.

2.6 Evaluation metrics

To evaluate the post-processed precipitation distributions from each of the three GPR post-processing models in each of the three target regions, we employ three strictly proper scoring rules (Gneiting and Raftery, 2007), which are the negative log-likelihood (NLL), the continuous rank probability score (CRPS) and the Brier score (BS) – defined next. For the CRPS and the BS, we calculate their associated skill

scores, CRPSS and BSS, respectively (e.g. Angus et al., 2024). These measure the improvement relative to the CRPS and BS for the raw WRF precipitation output, which is considered as our baseline. The BSS metric is used to assess the ability of different post-processing methods to capture various precipitation thresholds (0, 1, 10, 30 and 50 mm d⁻¹) that span the spectrum of precipitation events, ranging from no precipitation to very extreme events. The frequency and total number of events exceeding these thresholds are included in Table B1 (Appendix B), showing that 10, 30 and 50 mm d⁻¹ represent extreme precipitation events for which nevertheless some amount of observations are available (e.g. 0.33 %, 2.95 % and 0.68 % of the total number of events exceed the 30 mm d⁻¹ threshold at West UIB, East UIB and Central UGB, respectively), as opposed to higher thresholds such as 100 mm d⁻¹, which have less than 0.2 % of observations, i.e. too low to justify use of this threshold. In addition, we use the threshold-weighted CRPS (twCRPS; with precipitation thresholds of 10 and 30 mm d⁻¹) to further assess the tails of the predictive distributions, by calculating the associated skill score twCRPSS (see Appendix B). The CRPSS, BSS and twCRPS metrics are also used to evaluate the skill of WRF_{SF}. To complement this, we also use the mean squared error (MSE) and mean absolute error (MAE) to compare the performance of the post-processed precipitation distributions reduced to their mean values against WRF_{SF} outputs, by again calculating their associated skill scores, MSESS and MAESS (see Appendix B).

Moreover, to assess the trade-off between goodness of fit and model complexity, we consider several information criteria. In particular, we compute the Akaike information criterion (AIC; Akaike, 1973), its small-sample corrected version (AICc; Sugiura, 1978) and the Kullback information criterion (KIC; Cavanaugh, 1999). These criteria, which consider both the log-likelihood of the model and the number of parameters in the model, are defined in Appendix C. While our model evaluation primarily relies on cross-validation and proper scoring rules, these criteria offer a complementary perspective on overall model quality.

The NLL assesses the compatibility of probabilistic hindcasts with observed data, especially focusing on the probability of observed events under the predicted probability distributions. It is defined as the sum of the natural logarithms of the probability density function values at the observed data points:

$$\text{NLL} = -\frac{1}{M} \sum_{m=1}^M \log(p(y_m^{\text{obs}} | x_m)), \quad (7)$$

where M represents the number of observations, y_m^{obs} denotes the m th observed data point and $p(y_m^{\text{obs}} | x_m)$ is the value of the predicted probability density function evaluated at that observed data point. NLL is the optimisation criterion used during training and therefore lower values indicate better performance.

The CRPS also measures how well probabilistic prediction matches the observed data y_m^{obs} by measuring the distance between the predicted and observed cumulative distribution functions (CDFs). The CRPS is defined as the integral of the squared difference between the predicted CDF $F(y_m)$ and the observed empirical CDF, which is the Heaviside step function $H(y_m - y_m^{\text{obs}})$, over the entire range of possible values of y :

$$\text{CRPS} = \frac{1}{M} \sum_{m=1}^M \int_{-\infty}^{\infty} \left(F(y_m) - H(y_m - y_m^{\text{obs}}) \right)^2 dy_m. \quad (8)$$

Using this, the CRPSS is then calculated as

$$\text{CRPSS} = 1 - \frac{\text{CRPS}}{\text{CRPS}_{\text{WRF}}}, \quad (9)$$

where CRPS_{WRF} is the CRPS of the raw WRF precipitation output. Positive values of CRPSS indicate improved skill relative to the raw WRF output, with higher values indicating better performance. Note that for deterministic predictions (i.e. WRF and WRF_{SF}) the CRPS reduces to the mean absolute error between the predicted and observed values.

The BS (Wilks, 2006) measures the mean squared error between M pairs of precipitation occurrence probabilities π_m and binary observations r_m^{obs} ,

$$\text{BS} = \frac{1}{M} \sum_{m=1}^M (\pi_m - r_m^{\text{obs}})^2, \quad (10)$$

and allows for a detailed assessment of the predictive capacity across different levels of precipitation intensity. Using this, the BSS is calculated as

$$\text{BSS} = 1 - \frac{\text{BS}}{\text{BS}_{\text{WRF}}}, \quad (11)$$

where BS_{WRF} is the BS of the raw WRF precipitation output. Positive BSS values indicate an improved skill relative to the raw WRF output, with higher values indicating better performance.

Finally, we extend the performance assessment for the combined-region models (E2) as these showcase the benefits and challenges associated with leveraging data from different regions. For this, we pool together the E2 held-out predictions for all (three) regions and use reliability diagrams and receiver operating characteristic (ROC) curves (e.g. Angus et al., 2024). Reliability diagrams serve as a visual representation of the calibration accuracy of predicted probabilities for different precipitation levels (0, 1, 10 and 30 mm d⁻¹), extending the evaluation beyond pairwise-correspondence metrics such as NLL, CRPSS and BSS. Reliability diagrams display the relationship between predicted probabilities of precipitation exceeding a certain threshold and the actual observed frequencies, with a perfect agreement indicated by such a relationship falling along the diagonal line on the

graph. ROC curves offer an alternative perspective of probabilistic model performance across different precipitation levels (0.1, 1, 10 and 30 mm d⁻¹). In particular, ROC curves assess the ability of probabilistic predictions to discriminate an event from a non-event by plotting the hit rate (i.e. ratio between the number of correctly predicted events and the total number of events) against the false alarm rate (i.e. ratio between the number of wrongly predicted events and the total number of events) using different predicted probability thresholds to transform the probabilistic prediction into a binary prediction of occurrence (Wilks, 2006; Angus et al., 2024). To allow for a better graphical differentiation of the ROC curves for different precipitation events, data points with no observed precipitation are excluded from this analysis.

2.7 Feature ablation

To determine the most influential input variables for the three GPR post-processing models, we perform a feature ablation analysis for E2 (Zeiler and Fergus, 2014; Kokhlikyan et al., 2020). Feature ablation is a technique that replaces each input variable (or feature) in \mathbf{x}_m with a baseline value (in this case, zero) and measures the impact this has on the output vector $\boldsymbol{\theta}_m$. This is done for each of the $D = 26$ input variables from Table 2 by running the trained GPR models 26 times, each time with a different input variable in \mathbf{x}_m replaced by zero, thereby obtaining predictions $\boldsymbol{\theta}_m$ for each ablated-feature input configuration. For each feature, the average of the absolute value of the differences between the ablated-feature model predictions and the original model predictions is computed for each output variable, i.e. π , α and β .

3 Results

Figure 3 shows how differences between observed and WRF-simulated mean daily precipitation vary by region and with terrain elevation. In West UIB and Central UGB, WRF systematically overestimates precipitation for all stations, i.e. for the full elevation range of the stations. This overestimate is especially apparent in Central UGB, with station measurements showing values of around 2 mm d⁻¹, whereas WRF generally simulates 8–10 mm d⁻¹. In East UIB, WRF underestimates precipitation at low-elevation stations (below around 1000 m a.s.l.) and broadly overestimates it at higher elevations (especially above 2000 m a.s.l.). These results generally show that the WRF output is characterised by highly variable precipitation biases across the three target regions that are consistent with complex elevation and hydroclimatological dependencies, and therefore that generalising MOS post-processing at ungauged locations is likely to be challenging. In addition, Fig. B1 (Appendix B) shows the Pearson correlation coefficient between raw WRF-simulated and observed daily precipitation time series for the differ-

ent stations, showing that while regional differences exist (e.g. correlations in Central UIB, where stations are relatively close to each other, are higher than in East UIB and West UIB, where the distances between stations are larger) the pairwise correspondence (or synchrony) between WRF and observations is low, ranging between 0.1 and 0.5.

Table 3 evaluates the performance of the three GPR post-processing models (VGLM, MLP_S and MLP_L) for each experiment and region using NLL. For E1, which assesses separate-region models for each of the three target regions, both MLP models marginally outperform the VGLM model in all three regions, with MLP_L performing best. Similar results are also apparent for E2, which tests how combined-region models generalise to held-out locations within those regions. Comparison of E2 and E1 shows that the combined-region GPR models (E2) perform marginally better than the separate-region GPR models (E1) for East UIB, but are marginally poorer for West UIB and Central UGB. However, the NLL values for E1 and E2 for each region and each GPR model are very similar and only differ in the second decimal place, i.e. there is little difference between the performance of either the separate-region or combined-region models, as well as between the three GPR models. For E3, which is analogous to E2 except that the GPR models are trained using data from two regions combined together and tested on the third region, NLL values are much higher compared with E2, highlighting a considerable drop in performance in all three regions. For example, the NLL value for MLP_L for West UIB is 1.24 for E2 and 2.46 for E3. Additionally, in E3, the range of NLL values within each region is relatively wide compared with E2, indicating that GPR performance in E3 is more sensitive to the choice of model architecture. For example, for West UIB the NLL value is 1.50 for VGLM, 2.84 for MLP_S and 2.46 for MLP_L. For E4, which is analogous to E1 except that testing happens at locations with higher elevations than those seen by the models during training, the performance of all GPR models slightly drops compared with E1. However, the NLL values for E1 and E4 for West UIB and East UIB still only differ in the second decimal place. Here, MLP_S shows the best performance for West UIB and East UIB, while for Central UGB it is MLP_L that shows the best performance.

In terms of differences across all experiments and models for each region, NLL values in East UIB are lower than those in West UIB by around 0.1, while NLL values in West UIB are in turn lower than those in Central UGB by (typically) 0.2 to 0.3 (Table 3). This pattern highlights the dominance of regional variability, driven by the quality/bias of the raw WRF output and the amount of station data available. For example, East UIB has the best-performing models and also the highest number of daily precipitation measurements (364 713), with West UIB having the second best-performing models and also the second highest number of measurements (76 860), and finally Central UGB having the poorest per-

forming models and also the least number of measurements (15 152) (Table 1).

Table 4 extends the performance assessment by showing the CRPSS for the three GPR models. The CRPSS values are largely consistent with the NLL results. For example, both MLP models outperform VGLM in all three regions for E1 and E2, and MLP_L is the best overall performing model. The CRPSS values for E1 and E2 for each region are very similar and only differ in the second decimal place, which was also found for the NLL results. For E3, all three GPR models exhibit lower CRPSS values and larger differences between models compared with E2, i.e. consistent with the considerable performance drop in all three regions and a higher sensitivity to the choice of model architecture found by NLL results. However, as CRPSS values for the GPR models are relative to the reference CRPSS_{WRF}, the positive CRPSS values achieved still represent an improvement in skill relative to WRF. For E3, MLP_S performs best for West UIB and East UIB (in contrast to VGLM for West UIB and MLP_L for East UIB for the NLL results), while VGLM performs best for Central UGB (in agreement with the NLL results). For E4, the performance of all models slightly drops compared with E1, with the MLP_L model still performing best across all three regions (in contrast to MLP_S for West UIB and East UIB for the NLL results, but in agreement with MLP_L for Central UGB, for the NLL results). CRPSS values also display differences across all experiments and models for each region, with the highest values of ≈ 0.8 in Central UGB, followed by values of ≈ 0.6 for West UIB and finally ≈ 0.4 for East UIB. However, as CRPSS values are relative to (and thus influenced by) CRPSS_{WRF}, which varies for each region, they are therefore not directly comparable across regions.

Table 4 also shows CRPSS values for WRF_{SF}. For all experiments and regions, the CRPSS values for WRF_{SF} are lower than those for the GPR models, indicating that the performance of the GPR models is superior to that of WRF_{SF}. For example, for E1 and E4 the WRF_{SF} values for East UIB are close to zero (-0.07), but positive in West UIB (≈ 0.4) and Central UGB (0.69), i.e. indicating negligible improvement relative to the raw WRF output for East UIB, but some improvement for West UIB and Central UGB. This is probably related to the direction of WRF-simulated biases changing with elevation for East UIB, while for West UIB and Central UGB the biases are larger and unidirectional (Fig. 3), i.e. large and unidirectional biases are more easily post-processed and thus the scaling factor approach is also effective. For E2, WRF_{SF} exhibits CRPSS values close to zero, indicating negligible improvement relative to the raw WRF output. For E3, WRF_{SF} shows values close to zero for West UIB (-0.03) and Central UGB (-0.04), but positive values for East UIB (0.35).

Additionally, Tables B2 and B3 (Appendix B) show MESS and MAESS values, respectively, for all three GPR models as well as WRF_{SF}. The results yielded by these metrics are broadly in line with those for CRPSS and confirm

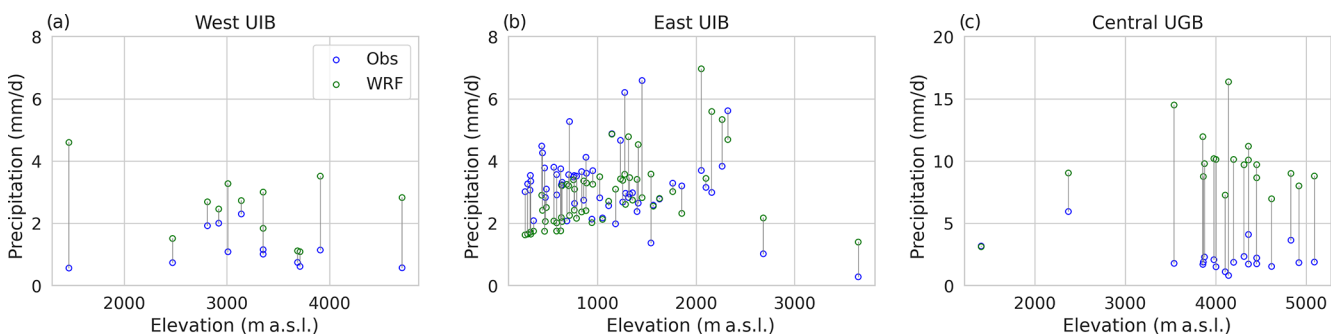


Figure 3. Difference between observed and WRF-simulated mean daily precipitation (mm d^{-1}) for each gauging station as a function of station elevation for (a) West UIB, (b) East UIB and (c) Central UGB.

Table 3. NLL values of post-processed daily WRF precipitation for the three GPR model architectures (VGLM, MLP_S and MLP_L), calculated for all four experiments and all three target regions. Lower NLL values indicate better performance, with the best-performing GPR model for each experiment and region shown in bold. NLL values are directly comparable across experiments and regions. Note that MLP_L for E3 West UIB was trained using a learning rate of 10^{-4} to ensure training convergence, while the other experiments used a learning rate of 10^{-3} .

Experiment	West UIB			East UIB			Central UGB		
	VGLM	MLP_S	MLP_L	VGLM	MLP_S	MLP_L	VGLM	MLP_S	MLP_L
E1	1.263	1.235	1.226	1.179	1.159	1.150	1.480	1.437	1.420
E2	1.267	1.245	1.240	1.181	1.156	1.144	1.501	1.477	1.448
E3	1.502	2.835	2.457	2.414	1.531	1.483	1.683	1.985	1.950
E4	1.283	1.250	1.251	1.187	1.160	1.173	1.875	1.553	1.511

that while the relative performance of GPR models varies depending on the assessment metric, the best-performing GPR models still outperform WRF_{SF} for all experiments and regions (except for E3 in East UIB, where MLP_S and WRF_{SF} yield the same MAESS value).

To better understand the performance of the GPR models for various precipitation intensities, Table 5 shows the BSS for the three GPR models for different daily precipitation thresholds. As expected, BSS values are consistent with CRPSS results but provide further granularity. For E1, E2 and E4, MLP_L is best at capturing the probability over low-to-moderate precipitation thresholds (i.e. 0, 1 and 10 mm d^{-1}), whereas results for higher precipitation events (i.e. 30 and 50 mm d^{-1}) are variable. However, for each region and threshold, the BSS values for different models generally only differ in the second decimal place, indicating that the performance of all GPR models is broadly similar for each region and threshold. For a threshold of 50 mm d^{-1} , smaller models generally perform marginally better for E1 (i.e. MLP_S in West UIB and East UIB and VGLM in Central UGB), E3 (MLP_S) and E4 (VGLM), whereas MLP_L performs best in E2 for East UIB and Central UGB. For E3, the VGLM model considerably outperforms the MLP models for low precipitation thresholds (i.e. 0 and 1 mm d^{-1}) in West UIB and Central UGB, whereas MLP_S performs best for higher thresholds (i.e. 30 and 50 mm d^{-1}) in these regions. Moreover, E3 also shows a much wider difference be-

tween models for West UIB and Central UGB. For example, for West UIB and a threshold of 30 mm d^{-1} , the BSS value is 0.47 for VGLM, 0.75 for MLP_S and 0.68 for MLP_L .

For all experiments and regions, the BSS values for WRF_{SF} are generally much lower than for the GPR models, indicating that the performance of the GPR models is superior to WRF_{SF} (i.e. consistent with the CRPSS results). However, for E1 and E4, WRF_{SF} can have BSS values that are comparable to the GPR models for higher thresholds, especially for East UIB and Central UGB. For example, for Central UGB, the BSS values for a threshold of 50 mm d^{-1} are 0.91 for MLP_L and 0.90 for WRF_{SF} .

In addition, Tables B4 and B5 (Appendix B) include twCRPSS values using 10 and 30 mm d^{-1} thresholds, respectively, for the three GPR models and WRF_{SF} . These results, which provide further insight regarding the ability of post-processing methods to capture extreme precipitation events, show that MLP models are best at characterising the tails of the predictive distributions in E1, E2 and E4 (excluding E2 for Central UGB in Table B5, where WRF_{SF} outperforms GPR models), whereas VGLM is the most robust option in E3. In West UIB and Central UGB, twCRPSS values for thresholds of 30 mm d^{-1} show all methods performing poorly; this can be explained by the relative lack of observations for events exceeding this threshold in both regions (Table B1).

Table 4. CRPSS values of post-processed daily WRF precipitation for the three GPR model architectures (VGLM, MLP_S and MLP_L) and WRF_{SF}, calculated for all three regions and all four experiments. Higher CRPSS values indicate better performance, with the best-performing MOS method for each experiment and region shown in bold. Positive CRPSS values indicate improved skill relative to raw WRF hindcasts. CRPSS values are directly comparable across experiments but not across regions. Note that MLP_L for E3 West UIB was trained using a learning rate of 10^{-4} to ensure training convergence, while the other experiments used a learning rate of 10^{-3} .

Experiment	West UIB				East UIB				Central UGB			
	VGLM	MLP _S	MLP _L	WRF _{SF}	VGLM	MLP _S	MLP _L	WRF _{SF}	VGLM	MLP _S	MLP _L	WRF _{SF}
E1	0.646	0.654	0.657	0.397	0.416	0.433	0.434	−0.075	0.820	0.823	0.824	0.691
E2	0.645	0.647	0.652	0.021	0.416	0.428	0.439	0.022	0.814	0.811	0.825	0.043
E3	0.491	0.585	0.556	−0.027	0.346	0.384	0.354	0.234	0.812	0.779	0.782	−0.039
E4	0.625	0.628	0.644	0.398	0.414	0.427	0.430	−0.073	0.808	0.818	0.818	0.690

Table 5. BSS values of post-processed daily WRF precipitation for the three GPR model architectures (VGLM, MLP_S and MLP_L) and WRF_{SF}, calculated for all three regions and all four experiments using a range of daily precipitation thresholds (0, 1, 10, 30 and 50 mm d^{−1}). Higher BSS values indicate better performance, with the best-performing MOS method for each experiment and region shown in bold. Positive BSS values indicate improved skill relative to raw WRF hindcasts. BSS values are directly comparable across experiments but not across regions.

Experiment	Threshold (mm)	West UIB				East UIB				Central UGB			
		VGLM	MLP _S	MLP _L	WRF _{SF}	VGLM	MLP _S	MLP _L	WRF _{SF}	VGLM	MLP _S	MLP _L	WRF _{SF}
E1	0	0.528	0.544	0.550	0.000	0.520	0.548	0.559	0.000	0.515	0.522	0.537	0.000
E1	1	0.484	0.502	0.511	0.110	0.390	0.426	0.441	−0.010	0.582	0.595	0.615	0.142
E1	10	0.748	0.753	0.753	0.554	0.403	0.425	0.428	−0.035	0.823	0.829	0.830	0.699
E1	30	0.746	0.752	0.744	0.667	0.448	0.456	0.451	−0.111	0.934	0.932	0.926	0.929
E1	50	0.686	0.692	0.680	0.667	0.461	0.465	0.457	−0.143	0.914	0.911	0.907	0.903
E2	0	0.528	0.529	0.538	0.000	0.524	0.550	0.561	0.000	0.474	0.497	0.522	0.000
E2	1	0.493	0.492	0.496	0.004	0.397	0.426	0.441	0.005	0.545	0.560	0.597	0.006
E2	10	0.747	0.748	0.752	0.024	0.404	0.419	0.433	0.012	0.820	0.810	0.825	0.020
E2	30	0.741	0.750	0.748	0.054	0.443	0.450	0.458	0.027	0.938	0.937	0.938	0.086
E2	50	0.679	0.692	0.672	0.060	0.457	0.461	0.465	0.048	0.917	0.917	0.919	0.101
E3	0	0.519	0.299	0.308	0.000	0.427	0.458	0.442	0.000	0.418	0.051	0.117	0.000
E3	1	0.485	0.331	0.338	−0.005	0.263	0.340	0.314	0.054	0.534	0.318	0.360	−0.003
E3	10	0.471	0.741	0.728	−0.028	0.326	0.375	0.329	0.172	0.817	0.811	0.808	−0.024
E3	30	0.473	0.745	0.680	−0.060	0.400	0.416	0.399	0.341	0.934	0.939	0.936	−0.074
E3	50	0.516	0.686	0.483	−0.090	0.432	0.438	0.431	0.410	0.916	0.916	0.912	−0.099
E4	0	0.521	0.534	0.546	0.000	0.519	0.544	0.555	0.000	0.441	0.461	0.501	0.000
E4	1	0.458	0.486	0.504	0.110	0.390	0.422	0.432	−0.010	0.566	0.556	0.577	0.142
E4	10	0.732	0.720	0.736	0.554	0.400	0.418	0.422	−0.035	0.806	0.824	0.826	0.688
E4	30	0.741	0.728	0.743	0.667	0.444	0.448	0.449	−0.111	0.938	0.939	0.932	0.926
E4	50	0.683	0.669	0.683	0.667	0.460	0.458	0.459	−0.143	0.916	0.916	0.908	0.903

Tables C3, C4 and C5 show how the three GPR models rank for each experiment and region, in terms of AIC, AICc and KIC, respectively. The rankings yielded by these metrics are generally consistent with the NLL results (Table 3), i.e. showing that MLP models tend to outperform VGLM models. These criteria penalise models with larger number of parameters (i.e. MLP_L; Table C2), especially in regions where the number of test data points is low (e.g. Central UGB and, to a lesser extent, West UIB; Table C1). AIC (Table C3) is the most lenient criterion, whereas AICc (Table C4) is more stringent with larger models and KIC (Table C5) penalises large models the most. Thus, in contrast to NLL results, MLP_S is favoured over MLP_L, except in East UIB, where

MLP_L ranks first for E2 (based on AIC, AICc and KIC) and E3 (based on AIC and AICc).

Figure 4 shows reliability diagrams and corresponding observed precipitation event histograms for daily precipitation thresholds exceeding 0, 1, 10 and 30 mm d^{−1} for E2, i.e. the combined-region model. For low precipitation thresholds (i.e. 0 and 1 mm d^{−1}), the reliability diagrams show that the majority of predicted probabilities are well-calibrated (Fig. 4a, b), as indicated by the data points correlating analogous levels to predicted probability and by the observed frequency of precipitation (dashed line) coinciding with the diagonal line (solid line). However, the calibration accuracy declines for predicted probability values of between 0.9 and

1.0 due to the model overpredicting the observed frequency. This occurs when the count of predicted instances for a given cumulative probability value decreases below a threshold of around 10^3 (Fig. 4e, f). This effect is even more evident for higher precipitation thresholds (i.e. 10 and 30 mm d⁻¹), where predicted probabilities and observed frequencies start to deviate at around 0.5 and 0.2, respectively (Fig. 4c, d), due to the model overpredicting the observed frequency. This also coincides with the number of predicted instances for these higher precipitation events dropping below a threshold of around 10^3 (Fig. 4g, h), highlighting the challenge of predicting extreme precipitation events.

Figure 5 displays ROC curves for daily precipitation thresholds exceeding 0.1, 1, 10 and 30 mm d⁻¹ for E2. This shows that GPR models exhibit superior binary classification accuracy, compared with raw WRF and WRF_{SF}, for all precipitation thresholds. This is graphically depicted in Fig. 5 by the (probabilistic) curves sitting considerably above the (deterministic) point values in the diagrams, indicating that the GPR models have higher true hit rates at equivalent or lower false alarm rates, compared with WRF and WRF_{SF}. Such a consistent pattern reinforces the evidence that GPR models not only provide a more nuanced forecast by quantifying uncertainty but also deliver a more reliable prediction in terms of discriminating between events and non-events for a given daily precipitation threshold. Additionally, Fig. 5 also shows for all precipitation thresholds that MLP_L consistently yields the best performance of the GPR models. Note that, for the ROC diagrams in Fig. 5, data points with no observed precipitation (i.e. dry days) are excluded from the analysis.

Figure 6 shows the effect that progressively adding input variables (listed in Table 2) has on GPR model performance for E2, in particular on the held-out NLL value for MLP_L. Starting with a set of core input variables (i.e. PRECIP, RAIN, DOY_{SIN}, DOY_{COS} and Z), the MLP_L model yields a held-out NLL value of 1.33 (configuration labelled “Core variables” in Fig. 6). By comparison, adding the spatial variables Y and X to the core set yields a held-out NLL value of 1.24 (labelled “+ Spatial variables”), while further adding the vertically integrated thermodynamic/cloud-related input variables WVP and CAPE to this configuration yields a value of 1.20 (labelled “+ Integrated variables”), i.e. indicating a systematic improvement in skill as the number of input variables increases. However, adding the temperature-related input variables T_{2m} , $T_{2m,MAX}$, $T_{2m,MIN}$ and $T_{2m,R}$ (labelled “+ Temperature variables”), and then further adding the horizontal and vertical wind-related input variables U_{10m} , V_{10m} , U_{500} , V_{500} , U_{250} , V_{250} , W_{500} and W_{250} (labelled “+ Wind variables”), results in held-out NLL values of 1.20, i.e. indicating negligible gain in skill compared with the “+ Integrated variables” configuration. By contrast, adding the relative humidity variables RH_{2m} and RH₅₀₀ further reduces the held-out NLL value to 1.18, which is likely to be due to these input variables being thermodynamic/cloud-related. Lastly, adding the remaining input variables GPH (i.e. WRF

orography), LU and YEAR yields a held-out NLL value of 1.18, i.e. no significant improvement.

Figure 7 assesses the relative influence that the input variables listed in Table 2 have on predicted outputs (i.e. the distributional parameters π , α and β) for the three GPR model architectures in E2. The feature importance analysis shows that the VGLM model is heavily influenced by a relatively limited set of input variables, whereas the MLP models (in particular MLP_L) leverage a more extensive array of predictors. The set of influential input variables is moderately consistent for all three output parameters. However, one notable exception is the dominant effect that T_{2m} has on π (Fig. 7a), but not on α and β (Fig. 7b, c), for the VGLM model. The results further show that, for all three GPR models, the vertically integrated thermodynamic/cloud variables (WVP and CAPE), the relative humidity variables (RH_{2m} and RH₅₀₀) and the near-surface temperature variables (T_{2m} , $T_{2m,MAX}$, $T_{2m,MIN}$ and $T_{2m,R}$) stand out as important features, as well as inputs such as LAT, Z and GPH. Moreover, and perhaps surprisingly, the precipitation input variables PRECIP and RAIN exhibit minimal influence on the GPR model outputs; this probably also explains the importance of the vertically integrated thermodynamic/cloud variables and the relative humidity variables, as these play a dominant role in controlling precipitation. Furthermore, the contribution of the horizontal and vertical wind velocity fields to the GPR outputs is also relatively minor. It is important to note that this feature ablation analysis does not assess multivariate effects, but only the effect that removing a single input variable (i.e. replacing it with zeros) has on the GPR model outputs. As a result, the lack of influence shown by certain variables could be due to these being redundant, given all other input variables (as evident in Fig. 6).

4 Discussion

4.1 Performance of GPR method for post-processing daily precipitation

In this study, we have shown that using a GPR approach to MOS post-processing (i.e. downscaling and bias-correcting) daily precipitation outputs from a reanalysis-driven RCM, for which simulated and observed daily precipitation data are expected to exhibit pairwise correspondence, improves predictions at ungauged locations across all tested regions, precipitation thresholds and experiments. We use three scoring metrics (NLL, CRPSS and BSS) to evaluate the quality of hindcasts and find that, overall, the three GPR models we employ (VGLM, MLP_S and MLP_L) exhibit similar performance (Tables 3, 4, 5) and consistently yield superior skill relative to the raw RCM output (WRF) and deterministic MOS bias correction (WRF_{SF}) (Tables 4, 5). We find that NLL (Table 3) and CRPSS (Table 4) yield similar relative rankings of GPR model performance. This is not surprising given that both the

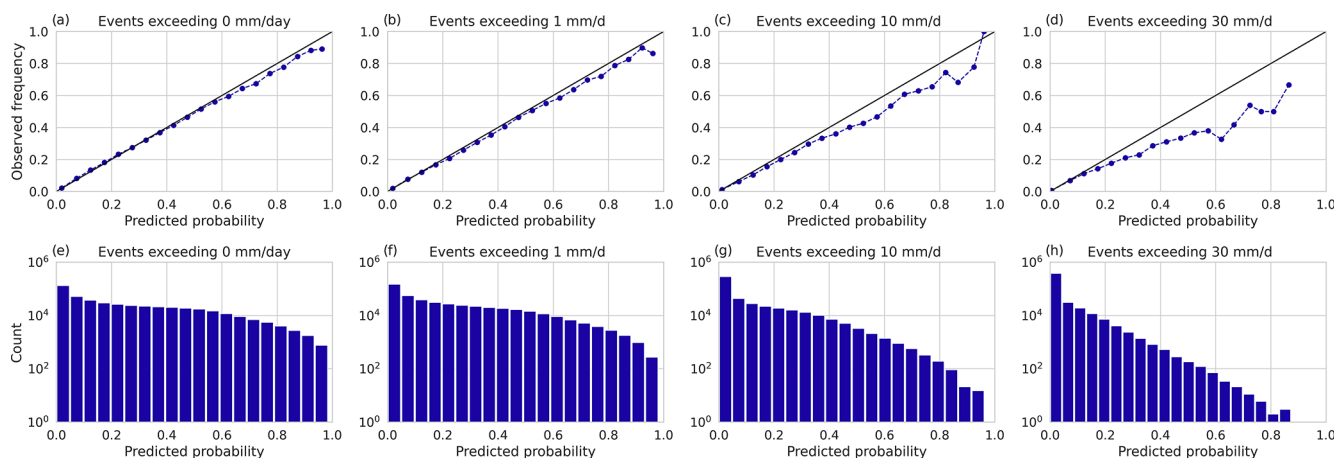


Figure 4. (a–d) Reliability diagrams and (e–h) predicted probability histograms for different observed daily precipitation thresholds: (a, e) 0.1 mm d^{-1} , (b, f) 1 mm d^{-1} , (c, g) 10 mm d^{-1} and (d, h) 30 mm d^{-1} . Reliability diagrams (a–d) display the relationship between predicted probabilities and the actual observed frequencies of precipitation exceeding a certain threshold (dotted line), with a perfect agreement indicated by the diagonal line (solid line). Predicted probability histograms (e–h) display the counts of observed events exceeding a certain threshold associated with various predicted probability levels.

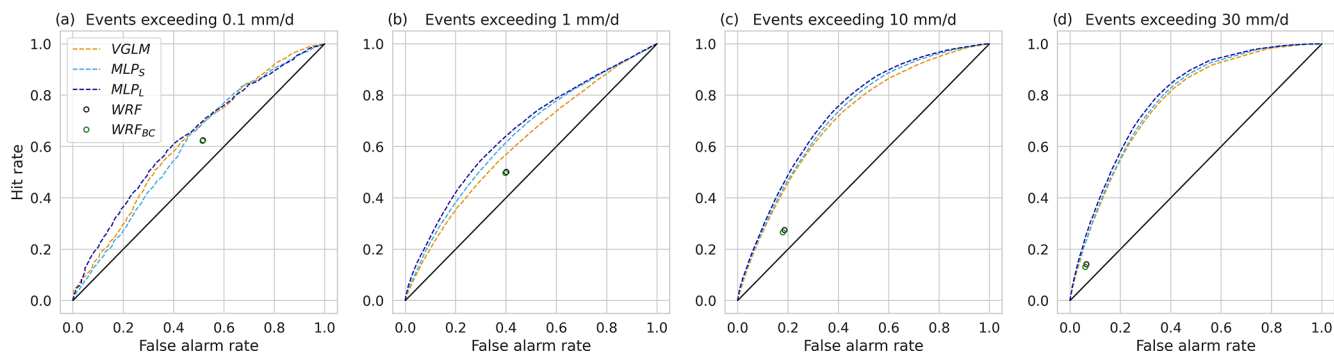


Figure 5. Receiver operating characteristic (ROC) curves yielded by the three GPR models, as well as hit rates and false alarm rates for WRF and WRF_{BC}, for different daily precipitation thresholds of (a) 0.1 mm d^{-1} , (b) 1 mm d^{-1} , (c) 10 mm d^{-1} , and (d) 30 mm d^{-1} . ROC curves exclude data points with no observed precipitation.

NLL and CRPS are strictly proper scoring rules that assess the goodness of fit of a predictive distribution against, in our case, a single observation and have their minima at the same value. However, the NLL is much more sensitive to extreme cases (as it involves a harsh penalty for events with low predicted probabilities) than the CRPS (Gneiting and Raftery, 2007). Therefore, it is insightful to corroborate the consistency of performance by using both scoring rules, whilst also noting that using the CRPS as the optimisation criterion for the GPR model parameters would have resulted in different GPR models and associated predictions. The BS assesses the accuracy of probabilistic predictions specifically for binary events. Whilst the CRPS is the integral of the BS over all real-valued probability thresholds and can therefore be viewed as a generalisation of the latter (Gneiting and Raftery, 2007), calculating the BS for specific precipitation thresholds provides additional granularity and shows insightful patterns for extreme precipitation events (Table 5).

MOS post-processing of RCM daily precipitation outputs at ungauged locations involves using separate groups of stations for model training, validation and testing. However, given the high spatial variability that daily precipitation exhibits both within and across regions, such an approach involves testing on out-of-distribution data, that is, models are assessed on their ability to generalise to held-out data that significantly deviate from the training data. This presents a particular challenge in representing extreme precipitation events. Daily precipitation in the three target regions is heavily skewed towards dry and very low precipitation amounts, with high-intensity precipitation events accounting for a very low fraction of the data (not shown). This imbalance hinders the models' ability to learn a robust representation of the probabilities associated with extreme precipitation events and how these vary spatially and temporally. For instance, the smaller/simpler GPR models, such as VGLM and MLP_S, stand out as more robust options for extreme precipitation

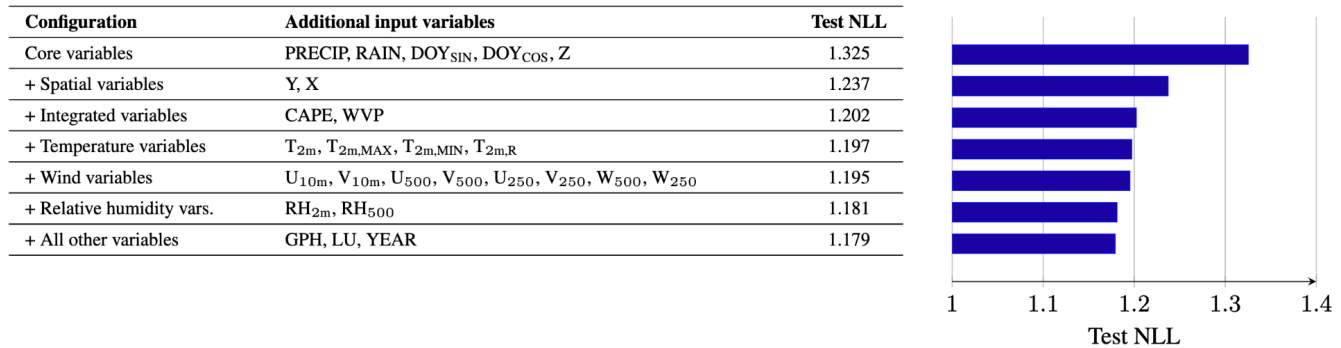


Figure 6. Test NLL yielded by MLP_L in E2 for different configurations of input variables. Each configuration includes all the input variables from the preceding rows in addition to the specific set of input variables listed for that configuration. For example, the configuration labelled “Core variables” comprises the input variables PRECIP, RAIN, DOY_{SIN}, DOY_{COS} and Z, whilst the configuration labelled “+ Spatial variables” comprises “Core variables” plus Y and X.

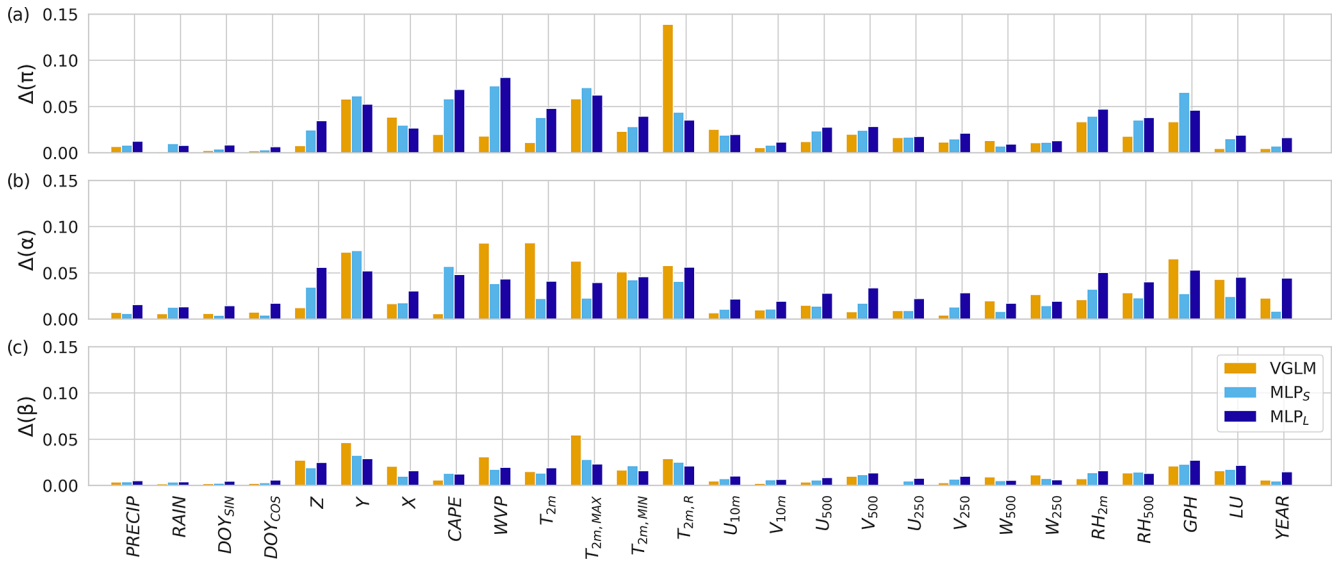


Figure 7. Feature ablation analysis for the three GPR models for E2, showing the effect that removing each input variable has on the output distributional parameters (a) π , (b) α and (c) β . Each vertical bar shows the average absolute-value output shift caused by ablating (i.e. replacing by zeros) a specific input variable, i.e. the larger the bar the more important the input variable is to the model.

events (Table 5), probably because they have fewer trainable parameters (Table C2) and are thus able to learn less intricate patterns from the training data. In this context, information criteria such as AIC, AICc and KIC (Tables C3, C4 and C5) emerge as complementary measures for comparing model quality (by balancing model performance and complexity); however, their interpretation for probably over-parametrised models (such as MLPs) is less straightforward because the effective number of parameters may be smaller than the nominal parameter count. In addition, given the variability of test set sizes across regions and experiments (Table C1), it is not clear which of these criteria is more appropriate, as each one of them has its own limitations and yields slightly different rankings. Therefore, we choose to interpret them with caution.

The four experiments we perform in this study assess GPR model performance across different post-processing tasks, which involve different ways of splitting data into training, validation and test sets. The dependencies between the training, validation and test datasets vary widely depending on whether the task involves a single region (E1) or multiple combined regions (E2), or extrapolating to either new regions (E3) or high elevations (E4). This explains the need for training models specific to each experiment and also highlights the spread of post-processing tasks considered in this work, attempting various degrees of generalisation. Consequently, the properties of the models trained to perform each task will also be different, which explains why GPR models ranked differently depending on the experiment.

In comparing GPR model performance across experiments, we showed that combined-region GPR models (E2) result in marginally better predictions than separate-region models (E1) for East UIB (Tables 3 and 4). Here, we hypothesise that East UIB benefits from combining data from all three regions because of the inherent challenges of this region, which is characterised by a complex bias-elevation distribution (Fig. 3), as well as an under-representation of station data at high-elevation bands (>2500 m a.s.l., Fig. 1). We also find that GPR models are capable of improving daily precipitation hindcasts in completely ungauged regions (E3) by leveraging data from other regions (Tables 4 and 5). This result contradicts with the assumption that, because RCM daily precipitation biases are region-specific (MauSSION et al., 2011; Norris et al., 2017; Bannister et al., 2019; ul Hassan et al., 2019), they are therefore not easily transferable to other regions. It is likely that GPR models are partially able to overcome this issue because, conditional on enough information (i.e. relevant input features), daily precipitation biases for different regions share some similarities. E4 explores GPR model generalisation to locations situated at higher elevations than the gauging stations used to train the models. We find that GPR models successfully post-process WRF precipitation for all regions and thresholds, exhibiting only a marginal performance drop relative to E1 (Tables 3, 4, 5). This finding is particularly important given that much of the high-elevation regions of HKH suffer from a profound lack of gauges (Pritchard, 2021; Thornton et al., 2022; Krishnan et al., 2019).

We find that training GPR models with progressively richer predictor configurations (i.e. with additional input variables, see Table 2) has a consistently positive effect on model performance, with some input variables (e.g. spatial, vertically integrated and relative humidity variables) driving most of the performance improvement (Fig. 6). Notwithstanding this, the performance gain yielded by incorporating additional input variables is strongly dependent on the previously added input variables. Thus, the relatively minor beneficial effect of variables such as temperatures and winds is likely to be only highlighting some degree of redundancy in the signal provided by different input variables. Furthermore, the three GPR models respond differently to the ablation of single input variables (Fig. 7); this highlights the complex interplay between input variables and model architecture. The reliance of the VGLM model architecture on a few input features contrasts the broader utilisation of inputs necessary for the MLP_L model. The influence exhibited by input variables such as elevation and latitude (i.e. representing topography), as well as convective available potential energy, water vapour and relative humidity (i.e. representing thermodynamics) for post-processing daily precipitation is in line with findings from previous studies showing that precipitation in this region is strongly associated with thermodynamic and dynamic interactions with topography (Orr et al., 2017; Potter et al., 2018; Bannister et al., 2019; Med-

ina et al., 2010; Ziarani et al., 2019; Dimri et al., 2017). In contrast, somewhat surprisingly, input variables such as total and liquid precipitation have little influence on output values (Fig. 7), which we hypothesise is partly due to the redundancy that exists between input variables, which in turn enables GPR models to compensate for the ablation of a single input variable by leveraging other variables.

4.2 Downstream use of GPR post-processed daily precipitation probability distributions

Probabilistic and deterministic predictions are inherently different and it is important to consider this when evaluating the quality of the products produced by both types of model. In this work, we are interested in assessing the performance of (probabilistic) GPR models, which leverage the pairwise correspondence between WRF daily precipitation output and observations, whilst capturing the predictive uncertainty that arises from multiple sources. A probabilistic MOS approach is justified if the goal is to fully leverage the richer predictions yielded by these models. For example, GPR model predictions can be used to map probabilities of exceedance for different precipitation thresholds (Fig. 8a, b, c), which form the basis of early warning systems (Reichstein et al., 2025), infrastructure planning (Salem et al., 2020) and climate risk analysis (Jones and Mearns, 2005). This is particularly relevant for mountainous areas with steep terrain (e.g. HKH), where extreme precipitation drives hydro-meteorological hazards such as floods or flash-floods, landslides and avalanches (Haslinger et al., 2025; Dimri et al., 2017; Hunt and Dimri, 2021). More generally, probabilistic outputs provide a calibrated uncertainty estimate for RCM-modelled daily precipitation at each spatio-temporal location, offering useful information to impact modellers, especially given that raw RCM precipitation hindcasts do not exhibit direct pairwise correspondence with observations (Fig. B1). Additionally, there are downstream impact modelling settings that are capable of leveraging probability distributions over precipitation. The latter is an emerging but largely untapped area of research for many impact modelling fields reliant on precipitation as one of the main inputs (e.g. hydrological and crop modelling; Li et al., 2013; Peleg et al., 2017). Conversely, if the intended use of the models is to essentially reduce the probabilistic predictions into a deterministic product, then deterministic metrics should be used to evaluate them. To this end, we use ROC curves to show that, for different precipitation thresholds, deterministic projections of GPR predictions still consistently outperform WRF and WRF_{SF} (Fig. 5).

Accurate representation of past and present-day daily precipitation holds significant importance for various downstream tasks, such as hydrological modelling, crop modelling or hazard analysis, all of which heavily rely on the hindcast precipitation for calibration. In hydrological modelling, knowing the distribution and timing of daily precip-

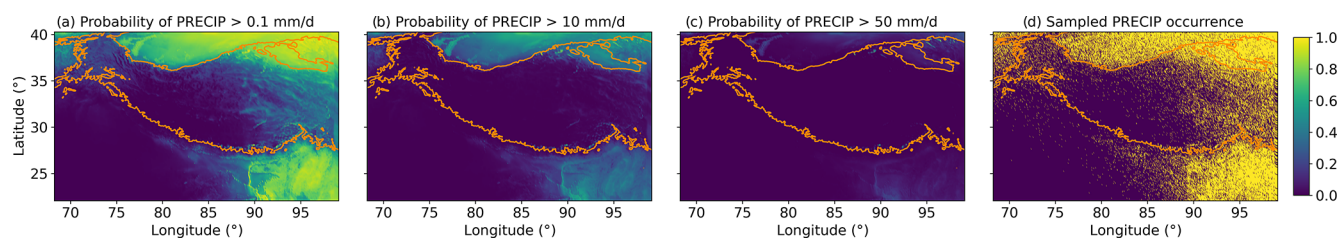


Figure 8. (a–c) Maps showing the probability of precipitation exceeding (a) 0.1 mm d^{-1} , (b) 10 mm d^{-1} and (c) 50 mm d^{-1} over the entire WRF spatial domain on an arbitrary date (1 January 2010) using the MLP_L post-processing model trained using one of the k -fold splits in E2. (d) Map of modelled precipitation occurrence based on independently drawn samples from each grid cell's predicted probability distribution for the entire WRF spatial domain on an arbitrary date (1 January 2010) using the MLP_L post-processing model trained using one of the k -fold splits in E2. The 3000 m a.s.l. contour is shown in orange in all four maps.

itation is crucial for simulating streamflow and predicting river flooding events (e.g. Andermann et al., 2011; Huang et al., 2019; Li et al., 2017; Wulf et al., 2016). Similarly, in crop modelling, precise knowledge of daily precipitation patterns enables accurate estimation of water availability and crop growth, leading to improved yield predictions and agricultural management decisions (Wit et al., 2005). In hazard analysis, past climate data are paired with historic events (e.g. glacial lake outburst floods; Shrestha et al., 2023) to be able to determine what precipitation intensity triggered them. However, most impact modelling frameworks rely on the availability of spatio-temporal coherent precipitation fields, which the GPR framework does not directly support. This is a limitation of this study and we discuss ways to address this in more detail next.

4.3 Limitations and future work

Local-scale variability of precipitation in HKH remains a challenge for MOS post-processing models aimed at ungauged locations. The diverse climatic conditions and complex terrain in the region result in contrasting precipitation patterns among nearby stations, which limits the degree to which patterns observed in one location are representative of nearby locations (Immerzeel et al., 2014; Orr et al., 2017; Bhardwaj et al., 2021; Ren et al., 2017; Dimri et al., 2017; Thayyen et al., 2013; Potter et al., 2018). Using different locations to train, validate and test models is a common strategy in spatial prediction settings but it can introduce model biases (Burt et al., 2024), especially when the distribution of the gauging stations is uneven. Furthermore, the reliability of daily precipitation measurements in mountainous areas is compromised by issues such as gauge undercatch (Pritchard, 2021). Such challenges hinder our ability to thoroughly test MOS models across an entire region and thus to gain confidence in their use for operational post-processing of RCM daily precipitation.

Another important limitation of the study relates to the lack of spatial coherence when sampling from the predicted probability distributions. The GPR post-processing approach, as implemented in this work, assumes that the

daily precipitation probability for each grid cell, conditional on a set of input features, is independent of its neighbours. This assumption, coupled with the large variability of precipitation in the region, leads to scattered precipitation occurrence maps when drawing independent samples from the predicted probability distribution at each location across the grid (Fig. 8d). There are several methods to introduce spatial and temporal coherence into probabilistic precipitation fields, including reordering techniques such as the Schaake Shuffle (Clark et al., 2004), as well as more advanced machine learning techniques such as latent variable models (Garnelo et al., 2018) and diffusion-based approaches (Yang et al., 2024; Turner et al., 2024). However, implementing these methods requires a reference dataset that captures realistic spatio-temporal correlations. In the context of HKH, given the sparse observational network, direct estimation of these dependencies from in situ observations is not feasible. Instead, all such methods must rely on a pseudo-observational dataset to reconstruct coherent structures. We argue that the raw WRF precipitation outputs, which capture spatio-temporal precipitation structures, provide a natural choice for this role. In the case of the Schaake Shuffle, the weak conditioning of the probabilistic predictions on raw WRF precipitation – this is evidenced by the low influence WRF precipitation has on model outputs (Fig. 7, which can in turn be explained by the low pairwise correspondence between observed and WRF-simulated daily precipitation (Fig. B1)) – supports using the RCM hindcast as the reference dataset for structured reordering. This method can be directly applied to a set of sampled values from the GPR output distributions at each location. Alternatively, (i) the GPR framework can be extended by conditioning the post-processed daily precipitation distributions on a latent variable defined across space (or any other dimension, e.g. elevation) to build correlations between neighbouring locations, e.g. using Gaussian processes (Rasmussen and Williams, 2006), or (ii) a diffusion model could be used to recover spatio-temporal coherent maps conditional on GPR-sampled precipitation fields. However, these approaches would also probably need to rely on the raw WRF

precipitation fields for pre-training and thus capturing the spatio-temporal correlations.

Accurate representation of extreme precipitation events is another challenging area. Machine learning and statistical methods inherently perform best where there are sufficient training data; however, by definition, extreme precipitation events are relatively data-sparse. This is a well-known limitation of data-driven approaches and results in increased uncertainty in predictions at high precipitation thresholds compared with low thresholds. This is particularly true in the HKH region, where there is a pressing need for more station-based datasets, which would in turn increase the amount of observations for extreme events. Future work could further explore the performance and added value of GPR post-processing for extreme precipitation events by focusing on a specific observed high-intensity precipitation event in the region.

Disaggregating results spatially and temporally is important to assess the extent to which different MOS post-processing models improve results at finer scales. In this work, we have presented results (dis)aggregated at the regional level, enabling an analysis of regional differences. However, further spatial granularity (e.g. at the station level) would potentially lead to a better understanding of model performance across different elevations and latitudes. Seasonality of precipitation also varies greatly across the three study regions. For example, the winter westerlies are responsible for much of the annual precipitation in West UIB, whilst East UIB and Central UGB are summer monsoon dominated (Bookhagen and Burbank, 2010; Palazzi et al., 2013; Dimri et al., 2015). Given their relevance when it comes to impacts on water resources, flooding and other rainfall-induced natural disasters, correctly post-processing dominating seasons for each region is another important aspect to assess. To some extent, optimising GPR models to perform best across all seasons inherently weights seasons by their relative significance. However, this work does not explicitly optimise models by season. This is therefore a direction that could be explored in future work.

Although we considered various parametric distributions for modelling the conditional probability over daily precipitation and found that the Bernoulli–gamma mixture model is a previously used, robust and effective choice (Williams, 1998; Cannon, 2008), we suggest that further work be focused on the study of distributions for modelling the probability over daily precipitation (conditional on a set of variables). Finally, as we have shown that RCM post-processing patterns learnt from one region may be relevant for post-processing other (poorly gauged or completely ungauged) regions, future effort should be devoted to investigating the benefits of applying transfer learning (Pan and Yang, 2010) and meta-learning (Vanschoren, 2018) techniques for mountainous/data-sparse regions like HKH, i.e. involving a model being pre-trained using data from a set of regions (es-

pecially those that are relatively data-rich, such as the Alps) and then fine-tuned for a different region or set of regions.

5 Conclusions

The compound effect of the local-scale variability and sparse observations that characterise daily precipitation in HKH poses a significant challenge when it comes to post-processing RCM outputs for ungauged locations. In this work, we address this issue by introducing a generalised probabilistic regression (GPR) approach to MOS post-processing (i.e. downscaling and bias-correcting) of RCM-simulated daily precipitation hindcasts for ungauged mountain locations using sparse in situ observations. We test the GPR approach across three HKH regions and four experiments that mimic real-world scenarios. These experiments explore the ability of GPR models to generalise to the following:

- i. ungauged locations within each region using separate-region models,
- ii. ungauged locations within each region using combined-region models,
- iii. an entirely ungauged region using combined-region models and
- iv. high-elevation ungauged locations within each region using separate-region models.

Overall, the three GPR model architectures we employ exhibit similar and consistently large performance improvements relative to both the WRF baseline and the WRF_{SF} deterministic bias correction approach. Vector generalised linear models (VGLMs) are found to be a robust choice for GPR-based post-processing of WRF daily precipitation but non-linear models (MLP_S and MLP_L) do, in most cases, lead to improved performance. We find that GPR models are able to learn from sparsely distributed (both spatially and temporally) in situ observations and to generalise to new locations, using both separate-region or combined-region training settings. Performance of separate-region and combined-region GPR models is largely similar, resulting in much improved skill relative to WRF and WRF_{SF}. Combined-region GPR models are also capable of generalising to new (completely ungauged) regions by leveraging data from other two regions. Although there is an expected drop in performance compared with other experiments, this experiment still results in large skill improvements relative to WRF and WRF_{SF}, with simpler model architectures being more robust choices in this setting. Furthermore, we explore the degree to which GPR models are effective at post-processing ungauged high-elevation locations and find that their performance is consistent with previous experiments, suggesting that this approach

could be used to better understand much of the ungauged high-elevation regions of HKH.

GPR model performance exhibits large regional variability, driven by a combination of factors, including the availability of in situ observations, performance/bias of WRF baseline and hydro-meteorological characteristics of each region. Simple GPR models are best for large precipitation events. The differential influence that input variables have for different GPR models underscores the complex interplay between input features and GPR model architecture, with thermodynamic/cloud-related input variables being especially important. Lastly, our results show that GPR models can use patterns learnt from one region to improve RCM post-processing in other regions and we therefore suggest/hypothesise that transfer learning and meta-learning may be promising approaches to leverage observations/-knowledge from data-rich mountain regions (e.g. Alps) to improve RCM post-processing in other (data-poor) regions.

Appendix A: Spike-and-slab mixture models

To explicitly model the probability over both precipitation occurrence (zero and non-zero values) and magnitude, we resort to a special type of mixture model called a spike-and-slab model. A spike-and-slab model for a random variable Y is a generative model in which Y attains some fixed value v (spike) or is drawn from a probability distribution p (slab).

To implement a spike-and-slab model, let us consider a set of inputs $x_{1:M}$ and outputs $y_{1:M}$. Now, let $r_{1:M}$ be a collection of M additional binary values, the m th of which is 1 if $y_m > 0$ and 0 if $y_m = 0$. Assume that observations $y_{1:M}$ are drawn from, respectively, a collection of random variables $Y_{1:M}$. Assume that $r_{1:M}$ is sampled independently from a Bernoulli distribution. Following that, y_m is 0 if r_m is 0, and sampled from a continuous distribution with support $(0, \infty)$ (e.g. gamma or log-normal) if r_m is 1. Below we detail the probabilistic models and associated conditional log-probability for various mixture models of this type.

If we choose a gamma distribution with parameters α_m and β_m to model the continuous part of the distribution, y_m is produced via the following probabilistic model:

$$r_m \sim \mathcal{B}(\pi_m),$$

$$(y_m | r_m = 1) \sim \Gamma(\alpha_m, \beta_m).$$

We call this model a Bernoulli–gamma mixture model, for which the conditional log-probability of the collection of $(y, r)_{1:M}$ value pairs is given by

$$\begin{aligned} \sum_{m=1}^M \log p(y_m, r_m | x_m) \\ &= \sum_{m=1}^M \log \mathcal{B}(r_m; \pi_m) \Gamma(y_m; \alpha_m, \beta_m)^{r_m} \\ &= \sum_{m=1}^M r_m [\log \pi_m + \log \Gamma(y_m; \alpha_m, \beta_m)] \\ &\quad + (1 - r_m) \log(1 - \pi_m). \end{aligned}$$

Appendix B: Additional results

B1 Daily precipitation thresholds

To justify the choice of precipitation intensity thresholds and illustrate the rarity of extreme precipitation events in the station data used in this study, Table B1 shows the percentage (and total number) of in situ observations exceeding specific daily precipitation thresholds, highlighting that (i) events exceeding 10 mm d^{-1} account for 2.56 % of the data in West UIB, 9.26 % in East UIB and 6.17 % in Central UGB; (ii) at higher thresholds (30 and 50 mm d^{-1}), observations are limited – especially for West UIB and Central UGB, where less than 1 % of observed events are above these thresholds; and (iii) events exceeding 100 mm d^{-1} are extremely rare in all three regions, with the total number of observations being too low to justify the use of this threshold.

Table B1. Percentage (and total number) of in situ observations that exceed, or are equal to, a threshold of daily precipitation, for various thresholds (mm d^{-1}).

Threshold (mm d^{-1})	West UIB	East UIB	Central UGB
0 (all events)	100 % (76 860)	100 % (364 713)	100 % (15 152)
1	26.00 % (19 983)	20.08 % (73 231)	28.30 % (4288)
10	2.56 % (1969)	9.26 % (33 779)	6.17 % (935)
30	0.33 % (252)	2.95 % (10 761)	0.68 % (103)
50	0.08 % (63)	1.24 % (4511)	0.26 % (39)
100	0.00 % (1)	0.22 % (788)	0.10 % (15)

B2 Additional evaluation metrics

The mean squared error (MSE) quantifies the squared difference between a set of predicted and observed value pairs. We calculate the MSE between the deterministic predictions y_m and the observations y_m^{obs} . For probabilistic predictions, we use the mean of the predicted probability distribution as the predicted value y_m :

$$\text{MSE} = \frac{1}{M} \sum_{m=1}^M \left(y_m - y_m^{\text{obs}} \right)^2. \quad (\text{B1})$$

Using this, the MSE skill score (MSESS) is calculated as

$$\text{MSESS} = 1 - \frac{\text{MSE}}{\text{MSE}_{\text{WRF}}}. \quad (\text{B2})$$

The mean absolute error (MAE) quantifies the absolute difference between a set of predicted and observed value pairs. For deterministic predictions, we calculate the MAE between the predicted values y_m and the observations y_m^{obs} . For probabilistic predictions, we use the mean values of the predicted probability distributions as predicted values y_m :

$$\text{MAE} = \frac{1}{M} \sum_{m=1}^M \left| y_m - y_m^{\text{obs}} \right|. \quad (\text{B3})$$

Using this, we calculate the MAE skill score (MAESS) as

$$\text{MAESS} = 1 - \frac{\text{MAE}}{\text{MAE}_{\text{WRF}}}. \quad (\text{B4})$$

The threshold-weighted CRPS (twCRPS; Gneiting and Ranjan, 2011) extends the CRPS by incorporating weight functions that emphasise specific portions of the predictive distribution. This modification allows for a tailored assessment of hindcast performance, particularly focusing on designated ranges within the support; in our case, extreme events with daily precipitation above a threshold value τ :

$$\text{twCRPS} = \frac{1}{M} \sum_{m=1}^M u(y_m^{\text{obs}}) \int_{-\infty}^{\infty} \left(F(y_m) - H(y_m - y_m^{\text{obs}}) \right)^2 dy_m. \quad (\text{B5})$$

where

$$u(y_m^{\text{obs}}) = \begin{cases} 0 & \text{if } y_m^{\text{obs}} < \tau \\ 1 & \text{if } y_m^{\text{obs}} \geq \tau \end{cases}. \quad (\text{B6})$$

Using this, the twCRPSS is then calculated as

$$\text{twCRPSS} = 1 - \frac{\text{twCRPS}}{\text{twCRPS}_{\text{WRF}}}. \quad (\text{B7})$$

Table B2. MSE skill score (MSESS) values of post-processed daily WRF precipitation for the three GPR model architectures (VGLM, MLP_S and MLP_L) and WRF_{SF}, calculated for all three regions and all four experiments. Higher MSESS values indicate better performance, with the best-performing MOS method for each experiment and region shown in bold. Note that MLP_L for E3 West UIB was trained using a learning rate of 10^{-4} to ensure training convergence, while the other experiments used a learning rate of 10^{-3} .

Experiment	West UIB				East UIB				Central UGB			
	VGLM	MLP _S	MLP _L	WRF _{SF}	VGLM	MLP _S	MLP _L	WRF _{SF}	VGLM	MLP _S	MLP _L	WRF _{SF}
E1	0.646	0.659	0.646	0.587	0.318	0.336	0.330	−0.161	0.795	0.806	0.793	0.791
E2	0.640	0.666	0.630	0.037	0.297	0.322	0.313	0.041	0.801	0.792	0.802	0.077
E3	0.111	0.513	0.400	−0.056	0.361	0.356	0.322	0.302	0.777	0.742	0.791	−0.073
E4	0.613	0.660	0.636	0.586	0.309	0.323	0.246	−0.153	0.798	0.803	0.802	0.790

Table B3. MAE skill score (MAESS) values of post-processed daily WRF precipitation for the three GPR model architectures (VGLM, MLP_S and MLP_L) and WRF_{SF}, calculated for all three regions and all four experiments. Higher MAESS values indicate better performance, with the best-performing MOS method for each experiment and region shown in bold. Note that MLP_L for E3 West UIB was trained using a learning rate of 10^{-4} to ensure training convergence, while the other experiments used a learning rate of 10^{-3} .

Experiment	West UIB				East UIB				Central UGB			
	VGLM	MLP _S	MLP _L	WRF _{SF}	VGLM	MLP _S	MLP _L	WRF _{SF}	VGLM	MLP _S	MLP _L	WRF _{SF}
E1	0.472	0.477	0.501	0.397	0.089	0.110	0.114	−0.075	0.725	0.729	0.731	0.691
E2	0.443	0.486	0.457	0.021	0.075	0.095	0.080	0.022	0.707	0.706	0.746	0.043
E3	0.133	0.532	0.543	−0.027	0.181	0.233	0.162	0.233	0.716	0.697	0.750	−0.039
E4	0.422	0.487	0.475	0.398	0.063	0.079	−0.006	−0.073	0.750	0.739	0.740	0.690

Table B4. Threshold-weighted CRPS skill score (twCRPSS) values at a threshold of 10 mm d^{-1} for post-processed daily WRF precipitation for the three GPR model architectures (VGLM, MLP_S and MLP_L) and WRF_{SF}, calculated for all three regions and all four experiments. Higher twCRPSS values indicate better performance, with the best-performing MOS method for each experiment and region shown in bold.

Experiment	West UIB				East UIB				Central UGB			
	VGLM	MLP _S	MLP _L	WRF _{SF}	VGLM	MLP _S	MLP _L	WRF _{SF}	VGLM	MLP _S	MLP _L	WRF _{SF}
E1	0.010	0.067	0.045	−0.058	0.221	0.245	0.260	−0.018	0.239	0.322	0.315	0.159
E2	0.009	0.042	0.056	0.001	0.225	0.243	0.272	0.003	0.228	0.244	0.259	0.036
E3	0.184	−0.193	−0.187	−0.002	0.134	0.100	0.109	−0.019	0.278	0.257	0.023	−0.033
E4	−0.010	0.035	0.044	−0.063	0.231	0.250	0.257	−0.018	0.122	0.222	0.261	0.157

Table B5. Threshold-weighted CRPS skill score (twCRPSS) values at a threshold of 30 mm d^{-1} for post-processed daily WRF precipitation for the three GPR model architectures (VGLM, MLP_S and MLP_L) and WRF_{SF} , calculated for all three regions and all four experiments. Higher twCRPSS values indicate better performance, with the best-performing MOS method for each experiment and region shown in bold.

Experiment	West UIB				East UIB				Central UGB			
	VGLM	MLP_S	MLP_L	WRF_{SF}	VGLM	MLP_S	MLP_L	WRF_{SF}	VGLM	MLP_S	MLP_L	WRF_{SF}
E1	−0.083	−0.002	−0.018	−0.109	0.126	0.147	0.166	0.006	−0.395	−0.275	−0.327	−0.421
E2	−0.082	−0.023	0.007	−0.006	0.137	0.146	0.183	−0.004	−0.393	−0.386	−0.396	−0.007
E3	0.093	−0.163	−0.139	0.004	0.009	−0.023	0.003	−0.095	0.278	0.257	−0.539	0.001
E4	−0.092	−0.031	−0.008	−0.113	0.136	0.148	0.167	0.006	−0.468	−0.382	−0.333	−0.423

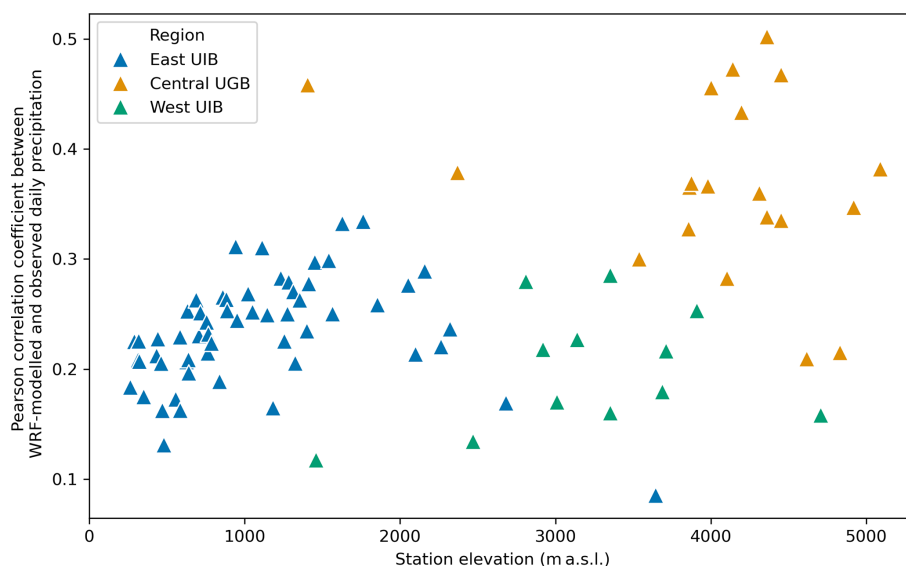


Figure B1. Pearson correlation coefficient between raw WRF-simulated and observed daily precipitation for each station, sorted by station elevation and coloured by region.

Appendix C: Information criteria for model selection

In order to assess the trade-off between the goodness of fit and model complexity, we consider various information criteria. In particular, we compute the Akaike information criterion (AIC; Akaike, 1973), as well as its small-sample corrected version (AICc; Sugiura, 1978) and the large-sample Kullback information criterion (KIC; Cavanaugh, 1999). These criteria are computed based on the maximum likelihood value and the number of parameters in the model. While our primary model evaluation relies on cross-validation and proper scoring rules, these criteria offer a complementary perspective, as discussed next.

The Akaike information criterion (AIC) is derived from an approximation of the Kullback–Leibler divergence between the true data generating process and a candidate model. It is given by

$$\text{AIC} = -2 \log L(\hat{\phi}) + 2k, \quad (\text{C1})$$

where $L(\hat{\phi})$ denotes the maximum likelihood of the model (with parameters ϕ) and k is the number of free parameters. A lower AIC value indicates a model that is closer, in the Kullback–Leibler sense, to the true model. Moreover, when the sample size n is small relative to the number of parameters k , the AIC tends to be biased. Therefore, a corrected version (AICc), given by

$$\text{AICc} = \text{AIC} + \frac{2k(k+1)}{n-k-1}, \quad (\text{C2})$$

is recommended in such cases. The AICc penalises models more strongly when n is only moderately larger than k . In the limit as $n \rightarrow \infty$, AICc converges to AIC.

The Kullback information criterion (KIC) is based on the symmetric version of the Kullback divergence and is defined as

$$\text{KIC} = -2 \log L(\hat{\phi}) + 3k. \quad (\text{C3})$$

By using a penalty term of $3k$ rather than $2k$, the KIC generally imposes a more severe penalty for model complexity, thereby favouring models with fewer parameters.

For each candidate model, we compute the total log-likelihood $\log L(\hat{\phi})$ by summing the per-observation contributions over the test set. In particular, we use the average per-observation negative log-likelihood (NLL) values in Table 3 and the number of test samples n in Table C1, to compute

$$\log L(\hat{\phi}) = -\overline{\text{NLL}} \times n.$$

(C4)

The information criteria are then computed via these expressions, with values of k specified in Table C2.

Table C1. Test set size n for each experiment and region.

Experiment	West UIB	East UIB	Central UGB
E1, E2, E3	76 860	364 713	15 152
E4	7189	26 847	1787

Table C2. Parameter count k for each candidate model.

GPR model	Parameter count (k)
VGLM	81
MLP _S	303
MLP _L	4053

Table C3. AIC values for the three GPR model architectures (VGLM, MLP_S and MLP_L), calculated for all four experiments and all three target regions. Lower AIC values indicate better quality, with the best GPR model for each experiment and region shown in bold.

Experiment	West UIB			East UIB			Central UGB		
	VGLM	MLP _S	MLP _L	VGLM	MLP _S	MLP _L	VGLM	MLP _S	MLP _L
E1	194 310	190 450	196 567	860 155	846 011	846 946	45 012	44 153	51 138
E2	194 925	191 987	198 719	861 614	843 822	842 569	45 648	45 365	51 986
E3	231 049	436 402	385 796	1 760 996	1 117 357	1 089 845	51 164	60 759	67 199
E4	18 609	18 578	26 093	63 897	62 891	71 089	6 863	6 156	13 506

Table C4. AICc values for the three GPR model architectures (VGLM, MLP_S and MLP_L), calculated for all four experiments and all three target regions. Lower AICc values indicate better quality, with the best GPR model for each experiment and region shown in bold. Note that AICc is not defined for $k > n$ (i.e. MLP_L for E4) and ND indicates “not defined”.

Experiment	West UIB			East UIB			Central UGB		
	VGLM	MLP _S	MLP _L	VGLM	MLP _S	MLP _L	VGLM	MLP _S	MLP _L
E1	194 310.53	190 452.61	197 018.08	860 155.29	846 011.24	847 037.02	45 012.80	44 165.26	54 098.73
E2	194 925.41	191 989.81	199 170.16	861 614.14	843 822.96	842 660.46	45 649.19	45 377.42	54 947.24
E3	231 049.61	436 404.61	386 247.40	1 760 996.40	1 117 357.71	1 089 935.87	51 164.51	60 771.85	70 159.85
E4	18 610.84	18 605.26	36 575.09	63 897.27	62 897.98	72 530.81	6 871.04	6 280.65	ND

Table C5. KIC values for the three GPR model architectures (VGLM, MLP_S and MLP_L), calculated for all four experiments and all three target regions. Lower KIC values indicate better quality, with the best GPR model for each experiment and region shown in bold.

Experiment	West UIB			East UIB			Central UGB		
	VGLM	MLP _S	MLP _L	VGLM	MLP _S	MLP _L	VGLM	MLP _S	MLP _L
E1	194 391	190 753	200 620	860 236	846 314	850 999	45 093	44 456	55 191
E2	195 006	192 290	202 772	861 695	844 125	846 622	45 729	45 668	56 039
E3	231 130	436 705	389 849	1 761 077	1 117 660	1 093 898	51 245	61 062	71 252
E4	18 690	18 882	30 146	63 978	63 194	75 142	6 944	6 459	17 559

Code and data availability. The code used to reproduce the experiments, generate figures and analyse the results presented in this study is available at <https://github.com/mgironamata/pddp-mountains> (Girona-Mata, 2025). The WRF simulation output is available via Norris et al. (2019). The SRTM elevation data are available at <https://earthexplorer.usgs.gov/> (NASA Shuttle Radar Topography Mission, 2013). In situ gauge datasets were collected and provided by the Bhakra Beas Management Board and the Indian Meteorological Department (East UIB), the Pakistan Meteorological Department and the Water and Power Development Authority (West UIB), and the International Centre for Integrated Mountain Development (Central UGB). The authors of this paper do not have the required permission to make the gauge datasets publicly available but suggest that any readers interested in obtaining them contact the above organisations.

Author contributions. MGM and AO defined the scope of the study. MGM conceptualised the probabilistic modelling approach with advice from SH and RET. MGM designed the experiments and conducted the research in close collaboration with AO, MW and RET. MGM and AO wrote the manuscript, with additional input from MW, RET, DB, DO, JN and JS. AO provided expertise on climate modelling, MW on post-processing and evaluation, and RET on probabilistic modelling and machine learning. DO and JS contributed to ensuring relevance for downstream applications. JN provided the WRF outputs. TP pre-processed the WRF outputs. DB, JS and GHD provided the observation datasets for East UIB, Central UGB and West UIB, respectively.

Competing interests. The contact author has declared that none of the authors has any competing interests.

Disclaimer. Publisher’s note: Copernicus Publications remains neutral with regard to jurisdictional claims made in the text, published maps, institutional affiliations, or any other geographical representation in this paper. While Copernicus Publications makes every effort to include appropriate place names, the final responsibility lies with the authors.

Acknowledgements. The authors are grateful to the two anonymous referees and the editor Alberto Guadagnini for their suggestions and insights.

Financial support. This research has been supported by UK Research and Innovation (grant no. EP/S022961/1; awarded to Marc Girona-Mata). Andrew Orr is supported by the UKRI/NERC grant “The Big Thaw: gauging the past, present and future of our mountain water resources” (grant no. NE/X005267/1). Richard E. Turner has been supported by the EPSRC Probabilistic AI Hub (grant no. EP/Y028783/1).

Review statement. This paper was edited by Alberto Guadagnini and reviewed by two anonymous referees.

References

- Akaike, H.: Information theory and an extension of the maximum likelihood principle, in: 2nd International Symposium on Information Theory, Akadémia Kiadó, Budapest, Hungary, edited by: Petrov, B. N. and Csáki, F., 2–8 September 1971, 267–281, 1973.
- Andermann, C., Bonnet, S., and Gloaguen, R.: Evaluation of precipitation data sets along the Himalayan front, *Geochim. Geophys. Geos.*, 12, Q07023, <https://doi.org/10.1029/2011GC003513>, 2011.
- Angus, M., Widmann, M., Orr, A., Ashrit, R., Leckebusch, G. C., and Mitra, A.: A comparison of two statistical postprocessing methods for heavy-precipitation forecasts over India during the summer monsoon, *Q. J. Roy. Meteor. Soc.*, 150, 1865–1883, <https://doi.org/10.1002/qj.4677>, 2024.
- Archer, D. R. and Fowler, H. J.: Spatial and temporal variations in precipitation in the Upper Indus Basin, global teleconnections and hydrological implications, *Hydrol. Earth Syst. Sci.*, 8, 47–61, <https://doi.org/10.5194/hess-8-47-2004>, 2004.
- Arfan, M., Lund, J., Hassan, D., Saleem, M., and Ahmad, A.: Assessment of spatial and temporal flow variability of the Indus River, *Resources*, 8, 103, <https://doi.org/10.3390/resources8020103>, 2019.
- Bannister, D., Orr, A., Jain, S. K., Holman, I. P., Momblanch, A., Phillips, T., Adeyoye, A. J., Snapir, B., Waine, T. W., Hosking, J. S., and Allen-Sader, C.: Bias Correction of High-Resolution Regional Climate Model Precipitation Output Gives the Best Estimates of Precipitation in Himalayan Catchments, *J. Geophys. Res.-Atmos.*, 124, 14220–14239, <https://doi.org/10.1029/2019JD030804>, 2019.
- Baño-Medina, J., Manzanar, R., and Gutiérrez, J. M.: Configuration and intercomparison of deep learning neural models for statistical downscaling, *Geosci. Model Dev.*, 13, 2109–2124, <https://doi.org/10.5194/gmd-13-2109-2020>, 2020.
- Baudouin, J. P., Herzog, M., and Petrie, C. A.: Contribution of cross-barrier moisture transport to precipitation in the upper indus river basin, *Mon. Weather Rev.*, 148, 2801–2818, <https://doi.org/10.1175/MWR-D-19-0384.1>, 2020.
- Beck, H. E., Wood, E. F., Pan, M., Fisher, C. K., Miralles, D. G., Dijk, A. I. V., McVicar, T. R., and Adler, R. F.: MSWEP V2 Global 3-hourly 0.1° Precipitation: Methodology and Quantitative Assessment, *B. Am. Meteorol. Soc.*, 100, 473–500, <https://doi.org/10.1175/BAMS-D-17-0138.1>, 2019.
- Bhardwaj, A., Wasson, R. J., Chow, W. T., and Ziegler, A. D.: High-intensity monsoon rainfall variability and its attributes: a case study for Upper Ganges Catchment in the Indian Himalaya during 1901–2013, *Nat. Hazards*, 105, 2907–2936, <https://doi.org/10.1007/s11069-020-04431-9>, 2021.
- Bolch, T., Kulkarni, A. V., Käab, A., Huggel, C., Paul, F., Cogley, J. G., Frey, H., Kargel, J. S., Fujita, K., Scheel, M., Bajracharya, S., and Stoffel, M.: The state and fate of Himalayan glaciers., *Science*, 336, 310–314, <https://doi.org/10.1126/science.1215828>, 2012.
- Bookhagen, B. and Burbank, D. W.: Toward a complete Himalayan hydrological budget: Spatiotemporal distribution of snowmelt and rainfall and their impact on river discharge, *J. Geophys. Res.-Earth*, 115, F03019, <https://doi.org/10.1029/2009JF001426>, 2010.
- Burt, D. R., Shen, Y., and Broderick, T.: Consistent Validation for Predictive Methods in Spatial Settings, *arXiv [preprint]*, <https://doi.org/10.48550/arXiv.2402.03527>, 2024.
- Cannon, A. J.: Probabilistic multisite precipitation downscaling by an expanded Bernoulli-gamma density network, *J. Hydrometeorol.*, 9, 1284–1300, <https://doi.org/10.1175/2008JHM960.1>, 2008.
- Cavanaugh, J. E.: A large-sample model selection criterion based on Kullback's symmetric divergence, *Stat. Prob. Lett.*, 42, 333–343, [https://doi.org/10.1016/S0167-7152\(98\)00200-4](https://doi.org/10.1016/S0167-7152(98)00200-4), 1999.
- Chinnasamy, P., Bharati, L., Bhattarai, U., Khadka, A., Dahal, V., and Wahid, S.: Impact of planned water resource development on current and future water demand in the Koshi River basin, Nepal, *Water Int.*, 40, 1004–1020, <https://doi.org/10.1080/02508060.2015.1099192>, 2015.
- Clark, M., Hay, L., Rajagopalan, B., and Wilby, R.: The Schaake Shuffle: A Method for Reconstructing Space-Time Variability in Forecasted Precipitation and Temperature Fields, *Tech. Rep.*, J. Hydrometeorol., 5, 243–262, 2004.
- Das, S., Ashrit, R., and Moncrieff, M. W.: Simulation of a Himalayan cloudburst event, *J. Earth Syst. Sci.*, 115, 299–313, <https://doi.org/10.1007/BF02702044>, 2006.
- Dimri, A. P.: Bias correction demonstration in two of the Indian Himalayan river basins, *J. Water Clim. Change*, 12, 1297–1309, <https://doi.org/10.2166/wcc.2020.119>, 2021.
- Dimri, A. P., Niyogi, D., Barros, A. P., Ridley, J., Mohanty, U. C., Yasunari, T., and Sikka, D. R.: Western Disturbances: A review, *Rev. Geophys.*, 53, 225–246, <https://doi.org/10.1002/2014RG000460>, 2015.
- Dimri, A. P., Chevuturi, A., Niyogi, D., Thayyen, R. J., Ray, K., Tripathi, S. N., Pandey, A. K., and Mohanty, U. C.: Cloudbursts in Indian Himalayas: A review, *Earth-Sci. Rev.*, 168, 1–23, <https://doi.org/10.1016/j.earscirev.2017.03.006>, 2017.
- Eden, J. M., Widmann, M., Grawe, D., and Rast, S.: Skill, correction, and downscaling of GCM-simulated precipitation, *J. Climate*, 25, 3970–3984, <https://doi.org/10.1175/JCLI-D-11-00254.1>, 2012.
- Garnelo, M., Schwarz, J., Rosenbaum, D., Viola, F., Rezende, D. J., Eslami, S. M. A., and Teh, Y. W.: Neural Processes, *arXiv [preprint]*, <https://doi.org/10.48550/arXiv.1807.01622>, 2018.
- Giorgi, F.: Thirty Years of Regional Climate Modeling: Where Are We and Where Are We Going next?, *J. Geophys. Res.-Atmos.*, 124, 5696–5723, <https://doi.org/10.1029/2018JD030094>, 2019.
- Girona-Mata, M.: mgironamata/pddp-mountains: v0.1.0 (v0.1.0), Zenodo [data set], <https://doi.org/10.5281/zenodo.1590332>, 2025.
- Gneiting, T. and Raftery, A. E.: Strictly proper scoring rules, prediction, and estimation, *J. Am. Stat. Assoc.*, 102, 359–378, <https://doi.org/10.1198/016214506000001437>, 2007.
- Gneiting, T. and Ranjan, R.: Comparing density forecasts using threshold and quantile-weighted scoring rules, *J. Bus. Econ. Stat.*, 29, 411–422, <https://doi.org/10.1198/jbes.2010.08110>, 2011.
- Haslinger, K., Breinl, K., Pavlin, L., Pistotnik, G., Bertola, M., Olefs, M., Greiling, M., Schöner, W., and Blöschl, G.: Increasing hourly heavy rainfall in Austria reflected in flood changes, *Nature*, 639, 667–672, <https://doi.org/10.1038/s41586-025-08647-2>, 2025.

- Hersbach, H., Bell, B., Berrisford, P., Hirahara, S., Horányi, A., Muñoz-Sabater, J., Nicolas, J., Peubey, C., Radu, R., Schepers, D., Simmons, A., Soci, C., Abdalla, S., Abellan, X., Balsamo, G., Bechtold, P., Biavati, G., Bidlot, J., Bonavita, M., Chiara, G. D., Dahlgren, P., Dee, D., Diamantakis, M., Dragani, R., Flemming, J., Forbes, R., Fuentes, M., Geer, A., Haimberger, L., Healy, S., Hogan, R. J., Hólm, E., Janisková, M., Keeley, S., Laloyaux, P., Lopez, P., Lupu, C., Radnoti, G., de Rosnay, P., Rozum, I., Vamborg, F., Villaume, S., and Thépaut, J. N.: The ERA5 global reanalysis, *Q. J. Roy. Meteor. Soc.*, 146, 1999–2049, <https://doi.org/10.1002/qj.3803>, 2020.
- Huang, Y., Bárdossy, A., and Zhang, K.: Sensitivity of hydrological models to temporal and spatial resolutions of rainfall data, *Hydrol. Earth Syst. Sci.*, 23, 2647–2663, <https://doi.org/10.5194/hess-23-2647-2019>, 2019.
- Huffman, G. J., Adler, R. F., Bolvin, D. T., Gu, G., Nelkin, E. J., Bowman, K. P., Hong, Y., Stocker, E. F., and Wolff, D. B.: The TRMM Multisatellite Precipitation Analysis (TMPA): Quasi-Global, Multiyear, Combined-Sensor Precipitation Estimates at Fine Scales, *J. Hydrometeorol.*, 8, 38–55, <https://doi.org/10.1175/JHM560.1>, 2007.
- Hunt, K. M. and Dimri, A. P.: Synoptic-scale precursors of landslides in the western Himalaya and Karakoram, *Sci. Total Environ.*, 776, 145895, <https://doi.org/10.1016/j.scitotenv.2021.145895>, 2021.
- Immerzeel, W. W., van Beek, L. P. H., and Bierkens, M. F. P.: Climate change will affect the Asian water towers, *Science*, 328, 1382–1385, <https://doi.org/10.1126/science.1183188>, 2010.
- Immerzeel, W. W., Petersen, L., Ragetti, S., and Pellicciotti, F.: The importance of observed gradients of air temperature and precipitation for modeling runoff from a glacierized watershed in the Nepalese Himalayas, *Water Resour. Res.*, 50, 2212–2226, <https://doi.org/10.1002/2013WR014506>, 2014.
- Immerzeel, W. W., Wanders, N., Lutz, A. F., Shea, J. M., and Bierkens, M. F. P.: Reconciling high-altitude precipitation in the upper Indus basin with glacier mass balances and runoff, *Hydrol. Earth Syst. Sci.*, 19, 4673–4687, <https://doi.org/10.5194/hess-19-4673-2015>, 2015.
- Iqbal, Z., Shahid, S., Ahmed, K., Ismail, T., and Nawaz, N.: Spatial distribution of the trends in precipitation and precipitation extremes in the sub-Himalayan region of Pakistan, *Theor. Appl. Climatol.*, 137, 2755–2769, <https://doi.org/10.1007/s00704-019-02773-4>, 2019.
- Ji, X., Li, Y., Luo, X., He, D., Guo, R., Wang, J., Bai, Y., Yue, C., and Liu, C.: Evaluation of bias correction methods for APHRODITE data to improve hydrologic simulation in a large Himalayan basin, *Atmos. Res.*, 242, 104964, <https://doi.org/10.1016/j.atmosres.2020.104964>, 2020.
- Jones, R. and Mearns, L.: Assessing future climate risks. Adaptation policy frameworks for climate change: Developing strategies, policies and measures, Tech. Rep., Cambridge University Press, Cambridge, UK, 119–143, 2005.
- Kingma, D. P. and Ba, J. L.: Adam: A method for stochastic optimization, in: 3rd International Conference on Learning Representations, ICLR 2015 – Conference Track Proceedings, 7–9 May 2015, San Diego, California, 2015.
- Klein, W. H. and Glahn, H. R.: Forecasting Local Weather by Means of Model Output Statistics, *B. Am. Meteorol. Soc.*, 55, 1217–1227, [https://doi.org/10.1175/1520-0477\(1974\)055<1217:flwbmo>2.0.co;2](https://doi.org/10.1175/1520-0477(1974)055<1217:flwbmo>2.0.co;2), 1974.
- Kokhlikyan, N., Miglani, V., Martin, M., Wang, E., Alsallakh, B., Reynolds, J., Melnikov, A., Kliushkina, N., Araya, C., Yan, S., and Reblitz-Richardson, O.: Captum: A unified and generic model interpretability library for PyTorch, Tech. Rep., arXiv, arXiv:2009.07896, <https://arxiv.org/abs/2009.07896> (last access: 1 September), 2020.
- Krishnan, R., Shrestha, A. B., Ren, G., Rajbhandari, R., Saeed, S., Sanjay, J., Syed, M. A., Vellore, R., Xu, Y., You, Q., and Ren, Y.: Unravelling Climate Change in the Hindu Kush Himalaya: Rapid Warming in the Mountains and Increasing Extremes, Springer International Publishing, 57–97, ISBN 978-3-319-92288-1, https://doi.org/10.1007/978-3-319-92288-1_3, 2019.
- Lafon, T., Dadson, S., Buys, G., and Prudhomme, C.: Bias correction of daily precipitation simulated by a regional climate model: a comparison of methods, *Int. J. Climatol.*, 33, 1367–1381, <https://doi.org/10.1002/joc.3518>, 2013.
- Li, H., Haugen, J. E., and Xu, C.-Y.: Precipitation pattern in the Western Himalayas revealed by four datasets, *Hydrol. Earth Syst. Sci.*, 22, 5097–5110, <https://doi.org/10.5194/hess-22-5097-2018>, 2018.
- Li, L., Gochis, D. J., Sobolowski, S., and Mesquita, M. D.: Evaluating the present annual water budget of a Himalayan headwater river basin using a high-resolution atmosphere-hydrology model, *J. Geophys. Res.*, 122, 4786–4807, <https://doi.org/10.1002/2016JD026279>, 2017.
- Li, Z., Brissette, F., and Chen, J.: Finding the most appropriate precipitation probability distribution for stochastic weather generation and hydrological modelling in Nordic watersheds, *Hydrol. Process.*, 27, 3718–3729, <https://doi.org/10.1002/hyp.9499>, 2013.
- Luo, X., Fan, X., Ji, X., and Li, Y.: Evaluation of corrected APHRODITE estimates for hydrological simulation in the Yarlung Tsangpo–Brahmaputra River Basin, *Int. J. Climatol.*, 40, 4158–4170, <https://doi.org/10.1002/JOC.6449>, 2020.
- Lutz, A. F., Immerzeel, W. W., Kraaijenbrink, P. D., Shrestha, A. B., and Bierkens, M. F.: Climate change impacts on the upper Indus hydrology: Sources, shifts and extremes, *PLoS ONE*, 11, e0165630, <https://doi.org/10.1371/journal.pone.0165630>, 2016.
- Maraun, D.: Bias correction, quantile mapping, and downscaling: Revisiting the inflation issue, *J. Climate*, 26, 2137–2143, <https://doi.org/10.1175/JCLI-D-12-00821.1>, 2013.
- Maraun, D. and Widmann, M.: Statistical Downscaling and Bias Correction for Climate Research, Cambridge University Press, ISBN 9788578110796, 2018.
- Maussion, F., Scherer, D., Finkelnburg, R., Richters, J., Yang, W., and Yao, T.: WRF simulation of a precipitation event over the Tibetan Plateau, China – an assessment using remote sensing and ground observations, *Hydrol. Earth Syst. Sci.*, 15, 1795–1817, <https://doi.org/10.5194/hess-15-1795-2011>, 2011.
- Medina, S., Houze, R. A., Kumar, A., and Niyogi, D.: Summer monsoon convection in the Himalayan region: Terrain and land cover effects, *Q. J. Roy. Meteor. Soc.*, 136, 593–616, <https://doi.org/10.1002/qj.601>, 2010.
- Momblanch, A., Papadimitriou, L., Jain, S. K., Kulkarni, A., Ojha, C. S., Adeloye, A. J., and Holman, I. P.: Untangling the water-food-energy-environment nexus for global change adaptation in a complex Himalayan water resource system, *Sci. Total Environ.*, 55, 1217–1227, [https://doi.org/10.1175/1520-0477\(1974\)055<1217:flwbmo>2.0.co;2](https://doi.org/10.1175/1520-0477(1974)055<1217:flwbmo>2.0.co;2), 1974.

- 655, 35–47, <https://doi.org/10.1016/j.scitotenv.2018.11.045>, 2019.
- Mukherji, A., Sinisalo, A., Nüsser, M., Garrard, R., and Eriksson, M.: Contributions of the cryosphere to mountain communities in the Hindu Kush Himalaya: A review, *Reg. Environ. Change*, 19, 1311–1326, <https://doi.org/10.1007/s10113-019-01484-w>, 2019.
- NASA Shuttle Radar Topography Mission (SRTM): Shuttle Radar Topography Mission (SRTM) Global, Earth Resources Observation and Science (EROS) Center [data set], <https://doi.org/10.5066/F7P7TFT>, 2013.
- Nepal, S., Steiner, J. F., Allen, S., Azam, M. F., Bhuchar, S., Biemans, H., Dhakal, M., Khanal, S., Li, D., Lutz, A., Pradhananga, S., Ritzema, R., Stoffel, M., and Stuart-Smith, R.: Consequences of cryospheric change for water resources and hazards in the Hindu Kush Himalaya Consequences of cryospheric change for water resources and hazards in the Hindu Kush Himalaya, in: ICIMOD, edited by: Wester, P., Chaudhary, S., Chettri, N., Jackson, M., an Mah, A., 73–121, <https://doi.org/10.53055/ICIMOD.1031>, 2023.
- Nie, Y., Pritchard, H. D., Liu, Q., Hennig, T., Wang, W., Wang, X., Liu, S., Nepal, S., Samyn, D., Hewitt, K., and Chen, X.: Glacial change and hydrological implications in the Himalaya and Karakoram, *Nature Reviews Earth and Environment*, 2, 91–106, <https://doi.org/10.1038/s43017-020-00124-w>, 2021.
- Norris, J., Carvalho, L. M., Jones, C., Cannon, F., Bookhagen, B., Palazzi, E., and Tahir, A. A.: The spatiotemporal variability of precipitation over the Himalaya: evaluation of one-year WRF model simulation, *Clim. Dynam.*, 49, 2179–2204, <https://doi.org/10.1007/s00382-016-3414-y>, 2017.
- Norris, J., Carvalho, L. M., Jones, C., and Cannon, F.: Deciphering the contrasting climatic trends between the central Himalaya and Karakoram with 36 years of WRF simulations, *Clim. Dynam.*, 52, 159–180, <https://doi.org/10.1007/s00382-018-4133-3>, 2019.
- Norris, J., Carvalho, L. M., Jones, C., and Cannon, F.: Warming and drying over the central Himalaya caused by an amplification of local mountain circulation, *npj Climate and Atmospheric Science*, 3, 1, <https://doi.org/10.1038/s41612-019-0105-5>, 2020.
- Orr, A., Listowski, C., Couttet, M., Collier, E., Immerzeel, W. W., Deb, P., and Bannister, D.: Sensitivity of simulated summer monsoonal precipitation in Langtang Valley, Himalaya, to cloud microphysics schemes in WRF, *J. Geophys. Res.*, 122, 6298–6318, <https://doi.org/10.1002/2016JD025801>, 2017.
- Orr, A., Ahmad, B., Alam, U., Appadurai, A. N., Bharucha, Z. P., Biemans, H., Bolch, T., Chaulagain, N. P., Dhaubanjari, S., Dimri, A. P., Dixon, H., Fowler, H. J., Gioli, G., Halvorson, S. J., Hussain, A., Jeelani, G., Kamal, S., Khalid, I. S., Liu, S., Lutz, A., Mehra, M. K., Miles, E., Momblanch, A., Muccione, V., Mukherji, A., Mustafa, D., Najmuddin, O., Nasimi, M. N., Nüsser, M., Pandey, V. P., Parveen, S., Pellicciotti, F., Pollino, C., Potter, E., Qazizada, M. R., Ray, S., Romshoo, S., Sarkar, S. K., Sawas, A., Sen, S., Shah, A., Shah, M. A. A., Shea, J. M., Sheikh, A. T., Shrestha, A. B., Tayal, S., Tigala, S., Virk, Z. T., Wester, P., and Wescoat, J. L.: Knowledge Priorities on Climate Change and Water in the Upper Indus Basin: A Horizon Scanning Exercise to Identify the Top 100 Research Questions in Social and Natural Sciences, *Earth's Future*, 10, e2021EF002619, <https://doi.org/10.1029/2021EF002619>, 2022.
- Palazzi, E., Hardenberg, J. V., and Provenzale, A.: Precipitation in the Hindu-Kush Karakoram Himalaya: Observations and future scenarios, *J. Geophys. Res.-Atmos.*, 118, 85–100, <https://doi.org/10.1029/2012JD018697>, 2013.
- Pan, S. J. and Yang, Q.: A survey on transfer learning, *IEEE T. Knowl. Data En.*, 22, 1345–1359, <https://doi.org/10.1109/TKDE.2009.191>, 2010.
- Peleg, N., Fatichi, S., Athanasios, P., Molnar, P., and Burlando, P.: An advanced stochastic weather generator for simulating 2-D high-resolution climate variables, *J. Adv. Model. Earth Sy.*, 9, 1595–1627, <https://doi.org/10.1002/2016MS000854>, 2017.
- Potter, E. R., Orr, A., Willis, I. C., Bannister, D., and Salerno, F.: Dynamical Drivers of the Local Wind Regime in a Himalayan Valley, *J. Geophys. Res.-Atmos.*, 123, 13186–13202, <https://doi.org/10.1029/2018JD029427>, 2018.
- Pritchard, H. D.: Global Data Gaps in Our Knowledge of the Terrestrial Cryosphere, *Frontiers in Climate*, 3, 1–7, <https://doi.org/10.3389/fclim.2021.689823>, 2021.
- Qazi, N. Q., Jain, S. K., Thayyen, R. J., Patil, P. R., and Singh, M. K.: Hydrology of the himalayas, Springer International Publishing, 419–450, ISBN 9783030296841, https://doi.org/10.1007/978-3-030-29684-1_21, 2019.
- Rasmussen, C. E. and Williams, C. K. I.: Gaussian Processes for Machine Learning, the MIT Press, ISBN 026218253X, 2006.
- Reichstein, M., Benson, V., Blunk, J., Camps-Valls, G., Creutzig, F., Fearnley, C. J., Han, B., Kornhuber, K., Rahaman, N., Schölkopf, B., Tárraga, J. M., Vinuesa, R., Dall, K., Denzler, J., Frank, D., Martini, G., Nganga, N., Maddix, D. C., and Weldemariam, K.: Early warning of complex climate risk with integrated artificial intelligence, *Nat. Commun.*, 16, 2564, <https://doi.org/10.1038/s41467-025-57640-w>, 2025.
- Ren, Y. Y., Ren, G. Y., Sun, X. B., Shrestha, A. B., You, Q. L., Zhan, Y. J., Rajbhandari, R., Zhang, P. F., and Wen, K. M.: Observed changes in surface air temperature and precipitation in the Hindu Kush Himalayan region over the last 100-plus years, *Advances in Climate Change Research*, 8, 148–156, <https://doi.org/10.1016/j.accre.2017.08.001>, 2017.
- Rumelhart, D. E., Hinton, G. E., and Williams, R. J.: Learning representations by back-propagating errors, *Nature*, 323, 533–536, <https://doi.org/10.1038/323533a0>, 1986.
- Sabin, T. P., Krishnan, R., Vellore, R., Priya, P., Borgaonkar, H. P., Singh, B. B., and Sagar, A.: Climate Change Over the Himalayas, Springer Singapore, 207–222, ISBN 9789811543272, https://doi.org/10.1007/978-981-15-4327-2_11, 2020.
- Sachindra, D. A., Ahmed, K., Rashid, M. M., Shahid, S., and Perera, B. J.: Statistical downscaling of precipitation using machine learning techniques, *Atmos. Res.*, 212, 240–258, <https://doi.org/10.1016/j.atmosres.2018.05.022>, 2018.
- Saha, S., Moorthi, S., Pan, H. L., Wu, X., Wang, J., Nadiga, S., Tripp, P., Kistler, R., Woollen, J., Behringer, D., Liu, H., Stokes, D., Grumbine, R., Gayno, G., Wang, J., Hou, Y. T., Chuang, H. Y., Juang, H. M. H., Sela, J., Iredell, M., Treadon, R., Kleist, D., Delst, P. V., Keyser, D., Derber, J., Ek, M., Meng, J., Wei, H., Yang, R., Lord, S., Dool, H. V. D., Kumar, A., Wang, W., Long, C., Chelliah, M., Xue, Y., Huang, B., Schemm, J. K., Ebisuzaki, W., Lin, R., Xie, P., Chen, M., Zhou, S., Higgins, W., Zou, C. Z., Liu, Q., Chen, Y., Han, Y., Cucurull, L., Reynolds, R. W., Rutledge, G., and Goldberg, M.: The NCEP Climate Forecast System Reanalysis, *B. Am. Meteorol. Soc.*, 91, 1015–1058, <https://doi.org/10.1175/2010BAMS3001.1>, 2010.

- Salem, S., Siam, A., El-Dakhkhni, W., and Tait, M.: Probabilistic Resilience-Guided Infrastructure Risk Management, *J. Manage. Eng.*, 36, 1–15, [https://doi.org/10.1061/\(asce\)me.1943-5479.0000818](https://doi.org/10.1061/(asce)me.1943-5479.0000818), 2020.
- Salzmann, N., Huggel, C., Rohrer, M., and Stoffel, M.: Data and knowledge gaps in glacier, snow and related runoff research – A climate change adaptation perspective, *J. Hydrol.*, 518, 225–234, <https://doi.org/10.1016/j.jhydrol.2014.05.058>, 2014.
- Samuel, J., Coulibaly, P., and Metcalfe, R. A.: Evaluation of future flow variability in ungauged basins: Validation of combined methods, *Adv. Water Resour.*, 35, 121–140, <https://doi.org/10.1016/j.advwatres.2011.09.015>, 2012.
- Sanjay, J., Krishnan, R., Shrestha, A. B., Rajbhandari, R., and Ren, G. Y.: Downscaled climate change projections for the Hindu Kush Himalayan region using CORDEX South Asia regional climate models, *Advances in Climate Change Research*, 8, 185–198, <https://doi.org/10.1016/j.accr.2017.08.003>, 2017.
- Shea, J. M., Wagon, P., Immerzeel, W. W., Biron, R., Brun, F., and Pellicciotti, F.: A comparative high-altitude meteorological analysis from three catchments in the Nepalese Himalaya, *Int. J. Water Resour. D.*, 31, 174–200, <https://doi.org/10.1080/07900627.2015.1020417>, 2015.
- Shrestha, F., Steiner, J. F., Shrestha, R., Dhungel, Y., Joshi, S. P., Inglis, S., Ashraf, A., Wali, S., Walizada, K. M., and Zhang, T.: A comprehensive and version-controlled database of glacial lake outburst floods in High Mountain Asia, *Earth Syst. Sci. Data*, 15, 3941–3961, <https://doi.org/10.5194/essd-15-3941-2023>, 2023.
- Shrestha, M., Acharya, S. C., and Shrestha, P. K.: Bias correction of climate models for hydrological modelling - are simple methods still useful?, *Meteorol. Appl.*, 24, 531–539, <https://doi.org/10.1002/met.1655>, 2017.
- Song, P. X.-K.: *Vector Generalized Linear Models*, Springer New York, 121–155, ISBN 978-0-387-71393-9, https://doi.org/10.1007/978-0-387-71393-9_6, 2007.
- Steiner, J. F., Gurung, T. R., Joshi, S. P., Koch, I., Saloranta, T., Shea, J., Shrestha, A. B., Stigter, E., and Immerzeel, W. W.: Multi-year observations of the high mountain water cycle in the Langtang catchment, Central Himalaya, *Hydrol. Process.*, 35, e14189, <https://doi.org/10.1002/hyp.14189>, 2021.
- Sugiura, N.: Further Analysis of the data by Akaike's information criterion and the finite corrections, *Communications in Statistics – Theory and Methods*, 7, 13–26, <https://doi.org/10.1080/03610927808827599>, 1978.
- Tazi, K., Orr, A., Hernandez-González, J., Hosking, S., and Turner, R. E.: Downscaling precipitation over High-mountain Asia using multi-fidelity Gaussian processes: improved estimates from ERA5, *Hydrol. Earth Syst. Sci.*, 28, 4903–4925, <https://doi.org/10.5194/hess-28-4903-2024>, 2024.
- Thayyen, R. J., Dimri, A. P., Kumar, P., and Agnihotri, G.: Study of cloudburst and flash floods around Leh, India, during August 4–6, 2010, *Nat. Hazards*, 65, 2175–2204, <https://doi.org/10.1007/s11069-012-0464-2>, 2013.
- Thornton, J. M., Pepin, N., Shahgedanova, M., and Adler, C.: Coverage of In Situ Climatological Observations in the World's Mountains, *Frontiers in Climate*, 4, 1–20, <https://doi.org/10.3389/fclim.2022.814181>, 2022.
- Turner, R. E., Diaconu, C.-D., Markou, S., Shysheya, A., Foong, A. Y. K., and Mlodozienec, B.: Denoising Diffusion Probabilistic Models in Six Simple Steps, arXiv [preprint], <https://doi.org/10.48550/arXiv.2402.04384>, 2024.
- ul Hasson, S., Böhner, J., and Chishtie, F.: Low fidelity of CORDEX and their driving experiments indicates future climatic uncertainty over Himalayan watersheds of Indus basin, *Clim. Dynam.*, 52, 777–798, <https://doi.org/10.1007/s00382-018-4160-0>, 2019.
- Vandal, T., Kodra, E., and Ganguly, A. R.: Intercomparison of machine learning methods for statistical downscaling: the case of daily and extreme precipitation, *Theor. Appl. Climatol.*, 137, 557–570, <https://doi.org/10.1007/s00704-018-2613-3>, 2019.
- Vanschoren, J.: Meta-Learning: A Survey, arXiv [preprint], <https://doi.org/10.48550/arXiv.1810.03548>, 2018.
- Vaughan, A., Tebbutt, W., Hosking, J. S., and Turner, R. E.: Convolutional conditional neural processes for local climate downscaling, *Geosci. Model Dev.*, 15, 251–268, <https://doi.org/10.5194/gmd-15-251-2022>, 2022.
- Wang, X., Tolksdorf, V., Otto, M., and Scherer, D.: WRF-based dynamical downscaling of ERA5 reanalysis data for High Mountain Asia: Towards a new version of the High Asia Refined analysis, *Int. J. Climatol.*, 41, 743–762, <https://doi.org/10.1002/joc.6686>, 2021.
- Wester, P., Mishra, A., Mukherji, A., and Shrestha, A. B.: The Hindu Kush Himalaya Assessment – Mountains, Climate Change, Sustainability and People, Springer Nature Switzerland AG, Cham, ISBN 9783319922874, https://doi.org/10.1007/978-3-319-92288-1_8, 2019.
- Widmann, M., Blake, R., Sooraj, K., Orr, A., Sanjay, J., Karumuri, A., Mitra, A., Rajagopal, E., Loon, A. F. V., Hannah, D., Barand, N., Singh, R., Mishra, V., Sudgen, F., and Arya, D.: Current opportunities and challenges in developing hydro-climatic services in the Himalayas: report of pump priming project November 2019, Tech. Rep., Centre for Ecology & Hydrology, Wallingford and Indian Institute of Tropical Meteorology, Pune, <https://nora.nerc.ac.uk/id/eprint/528847/> (last access: 1 September 2024), 2019.
- Wilks, D. S.: *Statistical Methods in the Atmospheric Sciences*, vol. 91, second edn., Elsevier Inc., ISBN 13: 978-0-12-751966-1, ISBN 10: 0-12-751966-1, 2006.
- Williams, P. M.: Modelling seasonality and trends in daily rainfall data, *Adv. Neur. In.*, 10, 985–991, 1998.
- Wit, A. J. W. D., Boogaard, H. L., and Diepen, C. A. V.: Spatial resolution of precipitation and radiation: The effect on regional crop yield forecasts, *Agr. Forest Meteorol.*, 135, 156–168, <https://doi.org/10.1016/j.agrformet.2005.11.012>, 2005.
- Wong, G., Maraun, D., Vrac, M., Widmann, M., Eden, J. M., and Kent, T.: Stochastic Model Output Statistics for Bias Correcting and Downscaling Precipitation Including Extremes, *J. Climate*, 27, 6940–6959, <https://doi.org/10.1175/JCLI-D-13-00604.1>, 2014.
- Wulf, H., Bookhagen, B., and Scherler, D.: Differentiating between rain, snow, and glacier contributions to river discharge in the western Himalaya using remote-sensing data and distributed hydrological modeling, *Adv. Water Resour.*, 88, 152–169, <https://doi.org/10.1016/j.advwatres.2015.12.004>, 2016.
- Xu, J., Badola, R., Chettri, N., Chaudhary, R. P., Zomer, R., Pokhrel, B., Hussain, S. A., Pradhan, S., and Pradhan, R.: *Sustaining Biodiversity and Ecosystem Services in the Hindu Kush Himalaya*, Springer International Publishing, 127–165, ISBN 978-3-319-92288-1, https://doi.org/10.1007/978-3-319-92288-1_5, 2019.

- Yang, Y., Jin, M., Wen, H., Zhang, C., Liang, Y., Ma, L., Wang, Y., Liu, C., Yang, B., Xu, Z., Bian, J., Pan, S., and Wen, Q.: A Survey on Diffusion Models for Time Series and Spatio-Temporal Data, arXiv [preprint], <https://doi.org/10.48550/arXiv.2404.18886>, 2024.
- Yatagai, A., Kamiguchi, K., Arakawa, O., Hamada, A., Yasutomi, N., and Kitoh, A.: APHRODITE: Constructing a Long-Term Daily Gridded Precipitation Dataset for Asia Based on a Dense Network of Rain Gauges, *B. Am. Meteorol. Soc.*, 93, 1401–1415, <https://doi.org/10.1175/BAMS-D-11-00122.1>, 2012.
- Zeiler, M. D. and Fergus, R.: Visualizing and Understanding Convolutional Networks, in: *Computer Vision – ECCV 2014*, edited by: David, F., Pajdla, T., Bernt, S., and Tinne, T., Springer International Publishing, 818–833, ISBN 978-3-319-10590-1, 2014.
- Ziarani, M. R., Bookhagen, B., Schmidt, T., Wickert, J., de la Torre, A., and Hierro, R.: Using convective available potential energy (CAPE) and dew-point temperature to characterize rainfall-extreme events in the South-Central Andes, *Atmosphere*, 10, 379, <https://doi.org/10.3390/atmos10070379>, 2019.